

# Unraveling hydrodynamization using ultracold 1D gases

Yicheng Zhang,<sup>1,2</sup> Yuan Le,<sup>3</sup> David S. Weiss,<sup>3</sup> and Marcos Rigol<sup>3</sup>

<sup>1</sup>*Homer L. Dodge Department of Physics and Astronomy,  
The University of Oklahoma, Norman, OK 73019, USA*

<sup>2</sup>*Center for Quantum Research and Technology, The University of Oklahoma, Norman, OK 73019, USA*

<sup>3</sup>*Department of Physics, The Pennsylvania State University, University Park, Pennsylvania 16802, USA*  
(Dated: June 25, 2024)

We study the quantum evolution of 1D Bose gases immediately after several variants of high-energy quenches, both experimentally and theoretically. Using the advantages conveyed by the relative simplicity of these nearly integrable many-body systems, we are able to differentiate the behavior of two distinct but often temporally overlapping processes, hydrodynamization and local prethermalization. There is a universal character to our findings, which can be applied to the short-time behavior of any interacting many-body quantum system after a sudden high-energy quench. We specifically discuss its potential relevance to heavy-ion collisions.

## I. INTRODUCTION

It is axiomatic in quantum mechanics that the unitary dynamics of a quantum state proceeds due to the relative evolution of the Bohr factors of the unchanging occupied eigenstates [1]. However, it is usually hard to get insight into the way any particular system evolves based on this high level view. Nearly integrable many-body systems are special cases in this regard, since they can be fully characterized in terms of very long lived quasiparticles that arise from interactions among particles. The momenta of these quasiparticles are known as rapidities, the distribution of which fully characterizes equilibrium states [2]. Rapidity distributions can be calculated in experimentally relevant models and they can be measured in 1D gases [3, 4]. In nearly integrable systems, consideration of the Bohr factors associated with quasiparticle states provides deep and surprisingly generic insights into the dynamics that follow a quantum quench.

The quasiparticle description provides the foundation for understanding “hydrodynamization” in nearly integrable gases of ultracold atoms in one dimension (1D) [5]. The term hydrodynamization was first introduced to describe the notably short period of time after the start of a relativistic heavy ion collision before hydrodynamics can be used to describe the time evolution of the system [6–12]. A characteristic feature of hydrodynamization is that energy gets redistributed among momentum modes that span the many-body system. Local thermalization, in contrast, involves redistribution among nearby momentum modes. The extent to which the two processes are temporally distinct depends on the details of the system and the quench, but it is generally the case that hydrodynamization runs its course before local thermalization is complete.

In Ref. [5], we showed that the time evolution after a large energy quench (implemented via a Bragg pulse) exhibits hydrodynamization before local prethermalization is completed. The quasiparticle picture allowed us to identify two time scales, hydrodynamization and momentum-dependent local prethermalization,

which scale with the Bragg momentum differently from each other. We conjectured in Ref. [5] that, since hydrodynamization occurs on very short time scales, far-from-integrable quantum systems that exhibit hydrodynamization may admit a quasiparticle description such as the one we used in near-integrable quantum systems. The quasiparticles, which account for strong correlations and explain the rapid energy transfer among widely separated momentum modes, do not have time to decay during hydrodynamization even if the system is far-from-integrable. We therefore expect that the understanding gained from consideration of nearly integrable 1D gases can be applied to generic interacting quantum systems in the short time immediately following a quench.

The first goal in this work is to explore the conditions necessary for hydrodynamization to occur in “high-energy” quenches, and to differentiate two characteristic time scales related to hydrodynamization: a single hydrodynamization coherence time  $T_{\text{hd}}^c$  identified in Ref. [5], and a hydrodynamization damping time  $T_{\text{hd}}^d$  that depends on the observable being considered. The second goal is to identify the times  $T_{\text{p}}$  associated with local prethermalization for different observables, and to explore local prethermalization in the presence and absence of hydrodynamization. We demonstrate, experimentally and theoretically, that the existence of distinct hydrodynamization epochs requires that there be a multimodal quasiparticle energy distribution after the quench. We consider two different quenches, a single Bragg pulse (as in Ref. [5]) and a quantum Newton’s cradle (QNC) sequence [13, 14]. Both quenches generate “high-energy” states with multimodal rapidity distributions, but only the single Bragg pulse generates a multimodal quasiparticle energy distribution. We show, experimentally and theoretically, that the single Bragg pulse leads to hydrodynamization, while the QNC sequence does not.

We then explore theoretically the extent to which a translationally invariant model reproduces the results of Bragg quenches in the presence of the trap. It turns out that the trap is not important, so we explore hydrodynamization and local prethermalization in a translationally invariant system. For that case, we directly write

the initial out-of-equilibrium many-quasiparticle state as a finite superposition of plane waves, rather than creating it with Bragg pulses. Our theoretical analysis shows that local prethermalization can occur very rapidly, regardless of whether or not there is hydrodynamization. We put to use the insights gained in this work to provide estimates for the hydrodynamization times and the fastest local prethermalization times in heavy-ion collisions.

The presentation is organized as follows. In Sec. II, we introduce the experimental setup and review its theoretical modeling. We also review our overall understanding of the quantum dynamics following a single Bragg pulse in a homogeneous Tonks-Girardeau gas. In Sec. III, we study the time evolution after a single Bragg pulse and after a QNC sequence, in both the experiment and the Tonks-Girardeau gas theory. We then explore theoretically, in Sec. IV, the effect on the hydrodynamization and local prethermalization time scales of density inhomogeneity due to the trapping potential and of finite Bragg pulse duration. In Sec. V, we use finite superpositions of plane waves in a translationally invariant model to explore in detail the necessary conditions for hydrodynamization and local prethermalization. We also determine how the local prethermalization rate for the momentum distribution depends on the specific superpositions considered. The potential relevance of our findings to heavy-ion collisions is discussed in Sec. VI. We summarize our results, and highlight open questions in Sec. VII.

## II. OVERVIEW

### A. Experiments and models

The experiment starts with a Bose-Einstein condensate of  $^{87}\text{Rb}$  atoms in the  $F = 1$ ,  $m_F = 1$  ground state confined in a red-detuned crossed dipole trap. We create a bundle of near-zero temperature 1D gases confined in separate “tubes” by adiabatically ramping up a blue-detuned 2D lattice to  $40E_r$  [15], where  $E_r = \hbar^2 k_0^2 / 2m$  is the recoil energy,  $k_0 = 2\pi / 775 \text{ nm}$  is the lattice wave vector, and  $m$  is the mass of a  $^{87}\text{Rb}$  atom. Theoretically, each individual tube can be modeled by adding a confining potential  $U(z)$  to the Lieb-Liniger Hamiltonian [16],

$$\mathcal{H}_{\text{LL}} = \sum_{j=1}^N \left[ -\frac{\hbar^2}{2m} \frac{\partial^2}{\partial z_j^2} + U(z_j) \right] + g \sum_{1 \leq j < l \leq N} \delta(z_j - z_l), \quad (1)$$

where  $N$  is the number of atoms in the tube, and  $g$  is the strength of contact interaction, which depends on the depth of the 2D lattice [17].  $U(z)$ , generated by the crossed dipole trap, is modeled as a Gaussian-shaped potential,

$$U(z) = U_0 \left[ 1 - \exp\left(-\frac{2z^2}{w^2}\right) \right], \quad (2)$$

where  $U_0$  is the depth of the Gaussian trap and  $w$  is its waist. The Lieb-Liniger Hamiltonian [Eq. (1) with

$U(z_j) = 0$ ] is exactly solvable via the Bethe ansatz [16, 18]. Observables in the equilibrium state only depend on the dimensionless parameter  $\gamma = mg / (\rho \hbar^2)$ , where  $\rho$  is the 1D atom density. For the trapped case, within the local density approximation (LDA), we consider the local  $\gamma(z) = mg / [\rho(z) \hbar^2]$  and define the average value of  $\gamma$  as  $\bar{\gamma} = \int dz \rho(z) \gamma(z) / [\int dz \rho(z)]$ . In what follows, we report the weighted average  $\bar{\gamma}_0$  of  $\bar{\gamma}$  in the initial state prior to the quenches in our array of 1D gases.

We carry out our theoretical analyses in the strong coupling Tonks-Girardeau (TG) limit ( $\gamma \rightarrow \infty$ ) of Hamiltonian (1), where out-of-equilibrium momentum and rapidity distributions can be readily calculated following Bragg scattering quenches. As shown in Ref. [5], the behavior in that limit is qualitatively similar to the experimental observations of hydrodynamization and local prethermalization at finite  $\gamma$ . In our numerical calculations, we use the low-density regime of the lattice hard-core boson Hamiltonian,

$$\mathcal{H}_{\text{HCB}} = -J \sum_{j=1}^{N_s-1} (\hat{b}_{j+1}^\dagger \hat{b}_j + \text{H.c.}) + \sum_{j=1}^L U(z_j) \hat{b}_j^\dagger \hat{b}_j, \quad (3)$$

where  $J$  is the hopping amplitude of a hard-core boson, and  $N_s$  is the total number of lattice sites. The boson creation (annihilation) operator  $\hat{b}_i^\dagger$  ( $\hat{b}_i$ ) creates (annihilates) a boson at lattice site  $i$ , and the hard-core constraint is enforced by  $\hat{b}_i^2 = \hat{b}_i^{\dagger 2} = 0$ . The position of site  $j$  on the lattice is set to be  $z_j = (j - N_s/2)a$ , with  $a$  the lattice spacing. In the limit in which the site occupation  $n_j = \langle \hat{b}_j^\dagger \hat{b}_j \rangle \rightarrow 0$  on all sites, the lattice hard-core boson Hamiltonian (3) is equivalent to the continuum Hamiltonian (1) in the TG limit [19]. The parameters of these two Hamiltonians are connected by  $J = \hbar^2 / (2ma^2)$ .

The main experimental observable is the momentum distribution  $f(p)$ , which is measured via a time-of-flight expansion [20] after the 1D interactions have been essentially turned off [3]. For the TG theory,  $f(p)$  is written as (up to a normalization constant)

$$f(p) \propto \langle \Psi_B | \hat{b}_p^\dagger \hat{b}_p | \Psi_B \rangle = \sum_{j,l} e^{ip(z_j - z_l) / \hbar} \langle \Psi_B | \hat{b}_j^\dagger \hat{b}_l | \Psi_B \rangle, \quad (4)$$

where  $\hat{b}_p^\dagger$  ( $\hat{b}_p$ ) creates (annihilates) a hard-core boson with momentum  $p$ , and  $|\Psi_B\rangle$  is the boson wave function. The in- and out-of-equilibrium equal-time correlation function  $\langle \Psi_B | \hat{b}_j^\dagger \hat{b}_l | \Psi_B \rangle$  can be efficiently computed by mapping the hard-core bosons onto noninteracting fermions via a Jordan-Wigner transformation [21],

$$\hat{b}_j^\dagger = \hat{c}_j^\dagger e^{-i\pi \sum_{l < j} \hat{c}_l^\dagger \hat{c}_l}, \quad (5)$$

where  $\hat{c}_j^\dagger$  ( $\hat{c}_j$ ) is the fermion creation (annihilation) operator at site  $j$ , and then using properties of Slater determinants [19, 22]. In the TG limit, the quasiparticles are the noninteracting fermions onto which the hard-core bosons are mapped. Therefore, the rapidity distribution

$f(\theta)$  is computed to be

$$f(\theta) \propto \langle \Psi_F | \hat{c}_\theta^\dagger \hat{c}_\theta | \Psi_F \rangle = \sum_{jl} e^{i\theta(z_j - z_l)/\hbar} \langle \Psi_F | \hat{c}_j^\dagger \hat{c}_l | \Psi_F \rangle, \quad (6)$$

where  $\hat{c}_\theta^\dagger$  ( $\hat{c}_\theta$ ) creates (annihilates) a noninteracting fermion with rapidity  $\theta$ , and  $|\Psi_F\rangle$  is the fermionic wave function.

## B. Single Bragg pulse

To create out-of-equilibrium states that feature hydrodynamization, we apply a Bragg pulse quench to the system [5] with a  $\lambda$  wavelength standing wave. That is, we turn on an additional potential,

$$U_{\text{pulse}}(z) = U_{\text{pulse}} \cos^2(kz), \quad (7)$$

with wavenumber  $k$  and amplitude  $U_{\text{pulse}}$ , for a short period of time  $t_{\text{pulse}}$ . In our experiments  $k \approx k_0$ , where  $k_0$  is the wavenumber of the 2D lattice. After the pulse, we let the system evolve in the initial trapping potential  $[U(z)$  in Eq. (2)] for different times  $t_{\text{ev}}$  and then measure the momentum distribution  $f(p)$ .

The effect of the Bragg pulse can be straightforwardly understood in the Raman-Nath regime ( $t_{\text{pulse}} \rightarrow 0$ ) for the homogeneous TG gas. The pulse in this regime, known as a Kapitza-Dirac pulse, “kicks” the particles and quasiparticles before they have had time to move. Such a kick generates a state in which the quasiparticles are in a superposition of plane waves that differ by even integer multiples of the Bragg momentum. The many-quasiparticle (noninteracting fermion) wave function changes from that of a Fermi sea  $|\Psi_0\rangle = \prod_{|\theta| < \theta_F} \hat{c}_\theta^\dagger |0\rangle$  to

$$|\Psi(t_{\text{ev}})\rangle = \prod_{|\theta| < \theta_F} \sum_n I_n(-ib) e^{-it_{\text{ev}}(\theta + n2\hbar k)^2/2m\hbar} \hat{c}_{\theta + n2\hbar k}^\dagger |0\rangle. \quad (8)$$

$I_n(-ib)$  are the modified Bessel functions of the first kind, where the integer  $n$  is the order of the Bragg peak and  $b$  depends on the area of the Bragg pulse [23]. In a homogeneous system, the rapidity distribution  $f(\theta)$  is conserved after the quench, but the momentum distribution  $f(p)$  for the bare particles evolves in time. The time evolution of the relative phases of different  $\hat{c}_\theta^\dagger$  enters  $f(p)$  via the Bose-Fermi mapping, so  $f(p)$  changes in time despite  $f(\theta)$  being constant. That is, although there is no redistribution of energy among the quasiparticles, there is a redistribution of energy among different momentum modes of the particles.

The largest relative energy difference between significantly populated quasiparticle states sets the fastest rate that  $f(p)$  can evolve. This is the “hydrodynamization coherence” time  $T_{\text{hd}}^c$ . Specifically, if the  $n = 0$  and  $\pm 1$  Bragg peaks are the mostly populated ones,

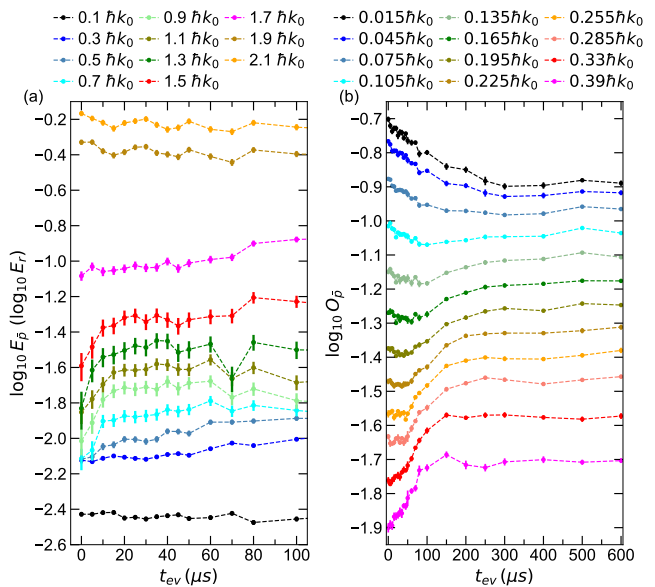


FIG. 1. *Experimental results from Ref. [5] for  $\bar{\gamma}_0 = 2.3$  after a  $6 \mu\text{s}$  Bragg pulse.* (a) Time evolution of  $E_{\bar{p}}$  [see Eq. (10)] with  $\Delta_p = 0.2\hbar k_0$ . (b) Time evolution of  $O_{\bar{p}}$  [see Eq. (12)] with  $\Delta_p = 0.03\hbar k_0$ . For the two curves with the highest  $\bar{p}$  in (b),  $\bar{p} = 0.33\hbar k_0$  and  $0.39\hbar k_0$ ,  $\Delta_p' = 0.06\hbar k_0$  and we report  $O_{\bar{p}}$  divided by 2. The hydrodynamization coherence time, see Eq. (9), is  $T_{\text{hd}}^c = 66 \mu\text{s}$ .

$\Delta E \simeq (2\hbar k)^2/2m$  and we have the characteristic frequency  $\omega_{\text{hd}}^c = \hbar(2k)^2/2m$  and corresponding period

$$T_{\text{hd}}^c = \frac{2\pi}{\omega_{\text{hd}}^c} = \frac{\pi m}{\hbar k^2}. \quad (9)$$

In Ref. [5], a pulse with  $t_{\text{pulse}} = 6 \mu\text{s}$  and  $U_{\text{pulse}} = 27 E_r$  was applied to systems with different values of  $U_0$  ( $2.6 E_r$ ,  $6.5 E_r$ , and  $22.9 E_r$ ), which correspond to different values of  $\bar{\gamma}_0$  ( $3.4$ ,  $2.3$ , and  $0.94$ ). The redistribution of energy among momentum modes was probed by studying the integrated kinetic energy per particle

$$E_{\bar{p}} = \int_{\bar{p}-\Delta_p/2}^{\bar{p}+\Delta_p/2} dp \frac{f(p)p^2}{2m}, \quad (10)$$

within the momentum intervals  $\Delta_p$  centered around  $\bar{p}$ . Figure 1(a) (adapted from Ref. [5]) shows that  $E_{\bar{p}}$  exhibits rapid changes across the momentum modes on the hydrodynamization time scale. For modes near the Bragg peaks this predominantly takes the form of damped oscillations with a frequency  $2\omega_{\text{hd}}^c$ , while for previously nearly unoccupied modes with momentum near  $\pm\hbar k$  there is an overdamped oscillation in which most of the energy transfer occurs in  $t_{\text{ev}} \lesssim T_{\text{hd}}^c/2$ . Theoretical calculations in the TG limit show complementary behavior in position space. The  $\lambda/2$ -scale variations of density generated by the Bragg pulse undergo damped oscillations with a frequency  $\omega_{\text{hd}}^c$  [5]. One can understand that the  $E_{\bar{p}}$  oscillation frequency is twice the spatial one because the phase of the underlying density distribution does not affect  $f(p)$ .

The damping of hydrodynamization oscillations in both position and momentum are a consequence of dephasing due to the spread ( $\theta_F$ ) in rapidities of the Bragg peaks. For the TG gas, the bandwidth of energy differences between the  $n = 0$  and  $\pm 1$  Bragg peaks associated with  $\theta_F$  is  $W = 8\hbar k\theta_F/(2m)$ , so the corresponding dephasing time scale is

$$T_{\text{dp}} = \frac{2\pi\hbar}{W} = \frac{\pi m}{2k\theta_F}. \quad (11)$$

Different bare-particle observables are associated with different combinations of quasiparticle operators. The specific way in which an observable evolves during hydrodynamization depends on the range, amplitudes, and relative phases of quasiparticle states that contribute to that observable. Therefore, we expect the hydrodynamization oscillations to damp in a time  $T_{\text{hd}}^d \propto T_{\text{dp}}$  for all observables, but with an observable-dependent coefficient. In Ref. [5], we found the damping of hydrodynamization oscillations for  $E_{\bar{p}}$  to occur in similar ways in similar times in the experiments and in the TG theory. For both experiment and TG theory, the evolution is fastest for  $E_{\bar{p}}$  of the originally little-occupied modes with momentum near  $\pm\hbar k$ . This suggests that those modes have relatively equal contributions from quasiparticle states across the rapidity range. With  $\theta_F$  as large as  $\hbar k$  in that work, the spread in hydrodynamization oscillation frequencies can be as large as  $\omega_{\text{hd}}^c$ , producing an overdamped oscillation in which  $T_{\text{hd}}^d \simeq T_{\text{hd}}^c$ .

Local prethermalization in the TG gas, which for  $f(p)$  describes the exchange of particles among nearby momentum modes, is also a consequence of dephasing due to the spread ( $\theta_F$ ) in rapidities of the Bragg peaks. Therefore, we also expect the local prethermalization time  $T_{\text{lp}}$  to be proportional to  $T_{\text{dp}}$  for all observables, as it is for the damping of hydrodynamization. However, the observable-dependent details of the time evolution are in general different from those associated with the damping of hydrodynamization. The fastest possible local prethermalization time is  $T_{\text{dp}}$ . This is the nearly momentum-independent prethermalization time of  $f(p)$  that we observe at high momenta. For momentum modes well within the central peak, the prethermalization time increases as  $p$  approaches 0 (see Sec. VA).

In Ref. [5], we found the prethermalization behavior of  $f(p)$  to be qualitatively similar in the experiment and in the TG gas theory. In Fig. 1(b) (adapted from Ref. [5]), we plot the occupation per particle

$$O_{\bar{p}} = \int_{\bar{p}-\Delta'_p/2}^{\bar{p}+\Delta'_p/2} dp f(p), \quad (12)$$

within the momentum intervals  $\Delta'_p$  centered around  $\bar{p}$ , measured experimentally. The experimental equilibration times of  $O_{\bar{p}}$  increase as  $\bar{p}$  decreases, as is also the case in the TG gas theory. It is also interesting to note that the local prethermalization times were nearly 3 times

longer in the experiments, suggesting that there is a dependence on the strength of the contact interaction  $g$  [see Eq. (1)] that is yet to be understood theoretically.

Summarizing our discussion in this section, we see that damping of hydrodynamization  $T_{\text{hd}}^d$  and local prethermalization  $T_{\text{lp}}$  both scale like  $T_{\text{dp}}$ , and they can both be understood with reference to dephasing quasiparticle states. They are, however, physically distinct processes. We will study these differences in the rest of this paper, taking advantage of our ability to turn on and off hydrodynamization, both in experiments and theory, and our ability to change both  $k$  and  $\theta_F$  in our theoretical calculations.

### III. HYDRODYNAMIZATION AND THE LACK THEREOF IN EXPERIMENT

#### A. A new single Bragg pulse

In the experimental results reported in this work, we use different pulses and pulse sequences to explore the hydrodynamization process and its absence under different conditions. Our single Bragg pulse has  $t_{\text{pulse}} = 10 \mu\text{s}$  and  $U_{\text{pulse}} = 18 E_r$ , and it is applied to a system that is initially in a trap with  $U_0 = 2.6 E_r$  and  $\bar{\gamma}_0 = 3.4$ . In Fig. 2(a), we plot our experimental results for the momentum distribution right after the Bragg pulse ( $t_{\text{ev}} = 0$ ), and at three later times. The most salient observation from these curves is that the momentum peaks broaden with time. In Figs. 2(b) and 2(c), we show theoretical results for the rapidity and momentum distributions, respectively, following the same Bragg pulse. The theory is for a single 1D gas in the TG limit with the same trap parameters as in the experiment. We set the atom number in the TG gas to be  $N = 29$ , so that the energy density per particle before the pulse is the same as in the experimental system for the bundle of tubes. One can see that the rapidity distribution [Fig. 2(b)] does not evolve significantly during the time in which the momentum distribution [Fig. 2(c)] does evolve. Since the experimental system has an array of tubes with different atom numbers and finite  $\gamma$ , we do not expect our theoretical results for a single tube with  $\gamma = \infty$  (initially in the ground state) to quantitatively match the experiment. Our goal is to espouse a simple theoretical description that allows us to qualitatively describe and understand the experimentally observed phenomena.

In Fig. 3(a), we plot our experimental results for  $E_{\bar{p}}$  [see Eq. (10)] as a function of  $t_{\text{ev}}$  for momentum intervals  $\Delta_p = 0.2\hbar k$ . As in the results in Ref. [5] [shown in Fig. 1(a)], for which a shorter but stronger Bragg pulse was used, the  $E_{\bar{p}}$  curves exhibit two clear features on the hydrodynamization coherence time scale  $T_{\text{hd}}^c = 66 \mu\text{s}$  [see Eq. (9)]. First, the curves with intermediate  $\bar{p}$  between the  $n = 0$  and  $\pm 1$  Bragg peaks ( $\bar{p}$  from  $0.5\hbar k$  to  $1.5\hbar k$ ) rise rapidly. Second, there are oscillations with a period that is close  $T_{\text{hd}}^c/2$ ; these are most clearly seen



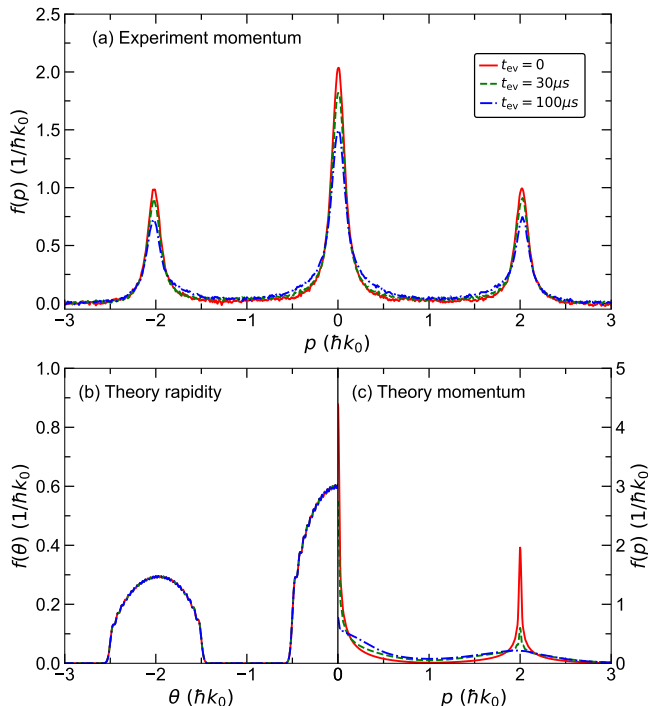


FIG. 2. Time evolution of the momentum and rapidity distributions after a  $10 \mu\text{s}$  Bragg pulse. (a) Experimental results for the momentum distribution for  $\bar{\gamma}_0 = 3.4$ . (b) and (c) Corresponding theoretical results for the rapidity (b) and momentum (c) distribution of a single 1D gas in the TG limit. In the theory, the trap parameters and the average energy per atom are the same as in the experiment before the quench.

in the curves with  $\bar{p}$  close to 0 or  $2\hbar k$ . The kinetic energy curves in Fig. 3(a) are qualitatively similar to those in Fig. 1(a), illustrating that the hydrodynamization process is robust. Small changes arise mostly because the difference in the experimental parameters modify  $T_{\text{dp}}$  (when  $\bar{\gamma}_0$  is greater,  $\theta_F$  is smaller).

In Fig. 3(b), we plot results from our numerical simulations of a single 1D gas in the TG limit with the same trap parameters as in the experiment. The theoretical  $E_{\bar{p}}$  curves capture the main experimental features. One can see both the rapid increase in the energies of the modes near  $\bar{p} \sim \hbar k$ , and the oscillations in energies of the modes with  $\bar{p}$  close to 0 or  $2\hbar k$ . Evidently, averaging over an array of 1D gases does not change the qualitative behavior of what occurs in a single tube. We note that the changes in the experimental curves are about half as large as those in the theoretical curves, possibly a result of averaging and possibly simply because the relationships between rapidities and momenta depend on the strength  $g$  of the contact interaction.

## B. QNC sequence

Equation (8) shows that each quasiparticle is in a superposition of plane waves with rapidities differing by

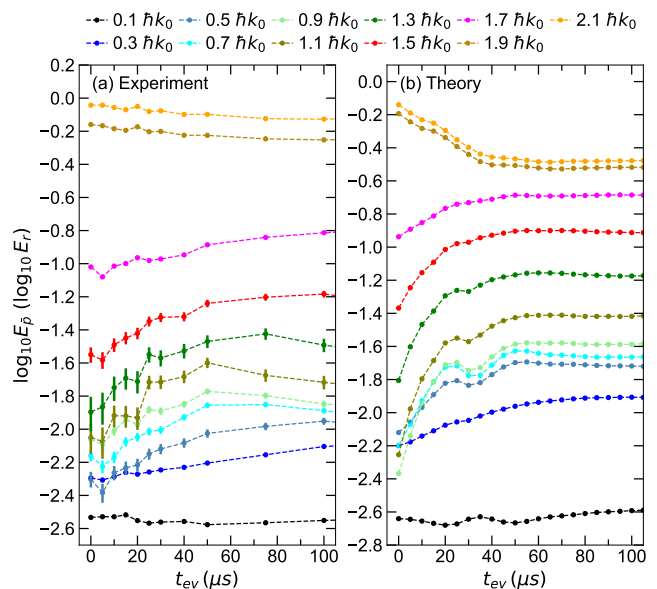


FIG. 3. Hydrodynamization after a  $10 \mu\text{s}$  Bragg pulse quench. Each curve shows the time evolution of the integrated energy  $E_{\bar{p}}$  over a  $0.2\hbar k$  wide momentum group [see Eq. (10)]. (a) Experimental results for  $\bar{\gamma}_0 = 3.4$ . (b) Theory calculation for a single 1D gas in the TG limit with the same trap parameters and average energy per atom as in the experiment before the quench. The dashed lines are guides to the eye.

$n2\hbar k$ . It also shows that the energy distribution of the quasiparticles after the Bragg pulse is multimodal, with peaks centered at energies  $(n2\hbar k)^2/2m$ . For the rapidity distribution obtained by modeling the experiment [see Fig. 2(b)], these peaks are well separated. As we argued using Eq. (8), the energy difference between the most populated  $n = 0$  and  $\pm 1$  Bragg peaks is the one that determines  $T_{\text{hd}}^c$ . We therefore expect that if the quasiparticles after the quench were to be in superpositions of plane waves with similar energies, say with  $n = \pm 1$ , there will be no hydrodynamization. In such a situation, the state after the quench is still “high-energy” compared to the ground state, since  $(2\hbar k)^2/2m$  remains the highest energy scale, yet there are no dynamics associated with that energy scale. The goal of this section is to confirm this expectation, showing that hydrodynamization is not an automatic outcome of dynamics after “high-energy” quenches.

A state in which the most populated Bragg peaks are the ones with  $n = \pm 1$  can be realized experimentally by applying a QNC sequence [13, 24]. The QNC sequence contains two Bragg pulses like the ones in Eq. (7). Optimal QNC pulses are  $\pi/(4\sqrt{2}\omega_r)$  long ( $23 \mu\text{s}$  for  $k_0$ ), separated by  $\pi/(4\omega_r)$  ( $33 \mu\text{s}$  for  $k_0$ ), where  $\omega_r = E_r/\hbar$  [13, 24]. These pulses are a large enough fraction of  $T_{\text{hd}}^c$  that significant hydrodynamization can occur during them. To reduce this effect, we use asymmetric QNC pulses. A long pulse followed by a short pulse still largely depletes the central peak, but at the cost of requiring a higher pulse amplitude, which compromises the two-level ap-

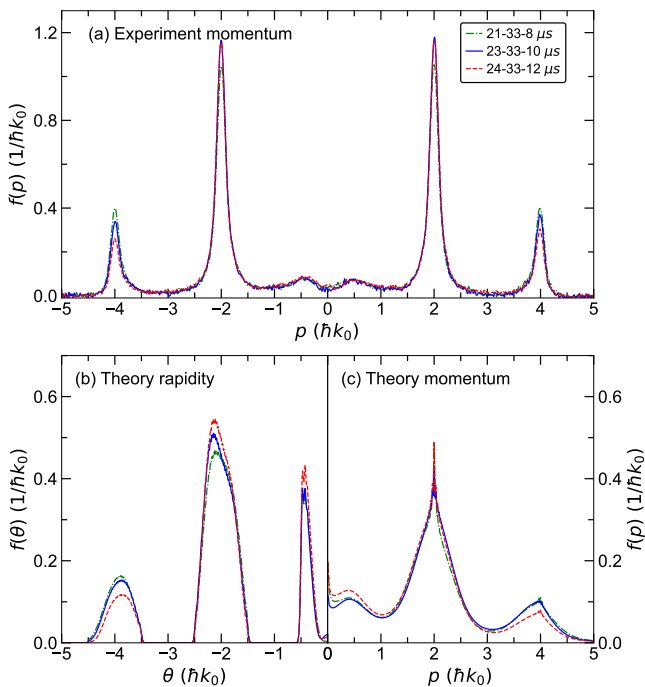


FIG. 4. Momentum and rapidity distributions at the end of different QNC sequences. Results are shown after three sequences with:  $t_{\text{pulse};1} = 21 \mu\text{s}$ ,  $t_{\text{mid}} = 33 \mu\text{s}$ , and  $t_{\text{pulse};2} = 8 \mu\text{s}$  (green dashed-dotted line);  $t_{\text{pulse};1} = 23 \mu\text{s}$ ,  $t_{\text{mid}} = 33 \mu\text{s}$ , and  $t_{\text{pulse};2} = 10 \mu\text{s}$  (blue solid line); and  $t_{\text{pulse};1} = 24 \mu\text{s}$ ,  $t_{\text{mid}} = 33 \mu\text{s}$ , and  $t_{\text{pulse};2} = 12 \mu\text{s}$  (red dashed line). (a) Experimental results for the momentum distribution. (b) and (c) Corresponding theoretical results for the rapidity (b) and momentum (c) distribution of a single 1D gas in the TG limit.

proximation that underlies the theory [24] and leads to a larger excitation of higher Bragg peaks. The advantage, however, is that there is less many-body evolution during the second pulse, so that the evolution after the second pulse presents a cleaner test of the absence of hydrodynamization. We label the amplitude and duration of the first (second) Bragg pulse as  $U_{\text{pulse};1}$  and  $t_{\text{pulse};1}$  ( $U_{\text{pulse};2}$  and  $t_{\text{pulse};2}$ ), respectively. We calculate these parameters assuming an ideal two-level system [24], which ignores many-body interactions. The ideal pulse separation is always the same as for symmetric pulses. For simplicity, we set  $U_{\text{pulse};1} = U_{\text{pulse};2}$ .

The length of the second pulse represents a trade-off between it being short and minimizing the  $|n| = 2$  excitations. Because many-body interactions complicate the ideal two-level system results in a way that is hard to calculate, we empirically determine a suitable QNC sequence. We start from the same pre-quench state (which is also the same as for the single Bragg pulse discussed in the previous subsection), and change the duration (and amplitude) of the two Bragg pulses. Figures. 4(a)–4(c) show respectively results for the momentum distributions obtained experimentally, and the rapidity and momentum distributions obtained theoretically, each after three different QNC sequences. The theoretical momentum

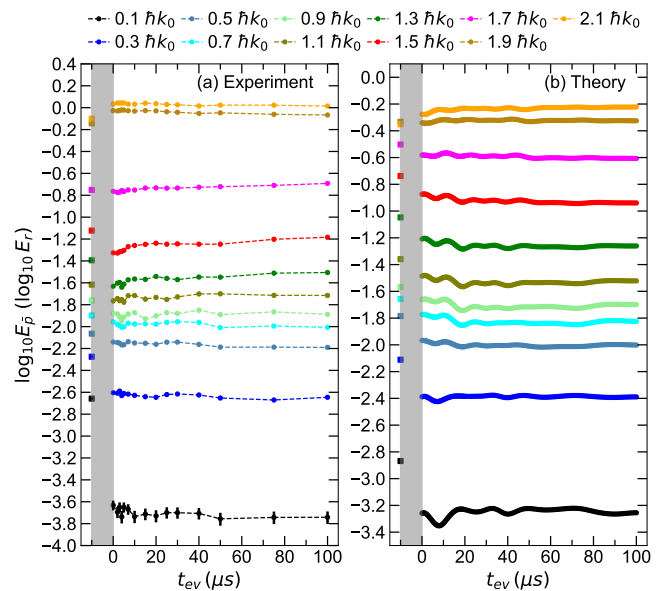


FIG. 5. Suppression of hydrodynamization after a QNC sequence. The curves show the time evolution of  $E_{\bar{p}}$ , in  $0.2\hbar k$  wide momentum intervals, following the QNC sequence with  $t_{\text{pulse};1} = 23 \mu\text{s}$ ,  $t_{\text{mid}} = 33 \mu\text{s}$ , and  $t_{\text{pulse};2} = 10 \mu\text{s}$ . On the  $x$  axis,  $t_{\text{ev}} = 0$  is the time at which the second Bragg pulse ends. We also plot, at  $t_{\text{ev}} = -10 \mu\text{s}$ , the values of  $E_{\bar{p}}$  at the beginning of the second pulse (the second pulse duration is indicated by the vertical gray band). (a) Experimental results for  $\bar{\gamma}_0 = 3.4$ . (b) Corresponding theoretical results for a single 1D gas in the TG limit, with the same trap parameters and energy density per particle as the experimental array of 1D gases. Dashed lines are guides to the eye.

distributions are qualitatively similar to the experimental ones, although the theoretical results exhibit lower and broader peaks than the experiment. Of the three QNC sequences, we choose to work with  $t_{\text{pulse};1} = 23 \mu\text{s}$ ,  $t_{\text{mid}} = 33 \mu\text{s}$ , and  $t_{\text{pulse};2} = 10 \mu\text{s}$  (blue solid line). When  $t_{\text{pulse};2}$  is shorter, the occupation of the  $n = \pm 1$  Bragg peaks starts to drop in favor of higher  $|n|$  peaks. Still, one can see that both in the experiment and the theory there are a nonnegligible number of atoms [and of quasiparticles in Fig. 4(b)] populating the  $n = \pm 2$  Bragg peaks. We further note from Fig. 4(b) that although the QNC sequences transfer nearly all quasiparticles with  $\theta \sim 0$  to higher rapidity modes, some quasiparticles with rapidities  $\theta \lesssim \theta_F$  remain. They are the reason there are small low-momentum side peaks in the experimental and theoretical momentum distributions about  $p = 0$ .

In Fig. 5, we plot the time evolution of  $E_{\bar{p}}$  after the 23-33-10  $\mu\text{s}$  QNC sequence in the experiment [Fig. 5(a)] and the corresponding theoretical results for a single 1D gas in the TG limit [Fig. 5(b)]. The grey shaded area indicates the time of the second ( $t_{\text{pulse};2} = 10 \mu\text{s}$ ) Bragg pulse in the sequence, which has the same amplitude and duration as the single Bragg pulse after which the dynamics are shown in Fig. 3. Figure 5 also shows, at  $t_{\text{ev}} = -10 \mu\text{s}$ , the values of  $E_{\bar{p}}$  at the beginning of the second pulse.

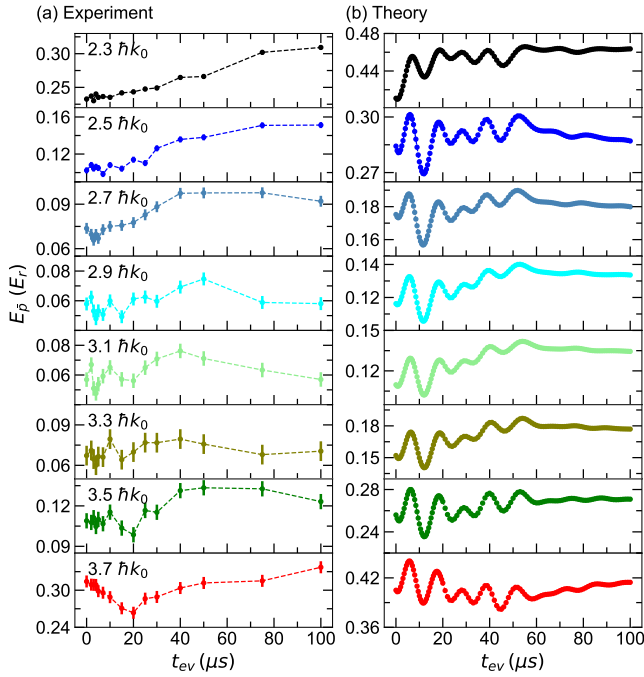


FIG. 6. *Hydrodynamization at higher momenta.* Time evolution of  $E_{\bar{p}}$  [see Eq. (10)] between  $2\hbar k_0$  and  $4\hbar k_0$ . The QNC sequence is the same as in Fig. 5, and we use  $0.2\hbar k$  wide momentum intervals to compute  $E_{\bar{p}}$ . (a) Experimental results for  $\bar{\gamma}_0 = 3.4$ . (b) Corresponding theoretical results for a single 1D gas in the TG limit, with the same trap parameters and energy density per particle as the experimental array of 1D gases. Dashed lines are guides to the eye.

The dominant effect of the second pulse is to deplete the  $n = 0$  peaks in the rapidity and momentum distributions. It also affects the occupation of the momentum modes between the  $n = 0$  and  $|n| = 1$  peaks, partially undoing the hydrodynamization evolution after the first pulse. Qualitatively, the system is far from equilibrium after the second pulse, as it would be after a single pulse of the same length. It just lacks the  $n = 0$  peak.

The experimental and the theoretical results for  $E_{\bar{p}}$  in Figs. 5(a) and 5(b), respectively, are qualitatively similar to each other for  $t_{ev} > 0$ . The curves are all relatively flat, with no oscillations with  $T_{hd}^c/2 = 33 \mu s$ , in stark contrast to the results due to the single pulse in Fig. 3. When the central peak is suppressed, so is hydrodynamization.

The curves in Fig. 5 feature oscillations with a higher frequency than that in Fig. 3. Such short time scale momentum mode changes are caused by the presence of atoms with  $n = \pm 2$  (see Fig. 4). In Fig. 6, we show our experimental [Fig. 6(a)] and theoretical [Fig. 6(b)] results for  $E_{\bar{p}}$  of momentum modes between  $2\hbar k_0$  and  $4\hbar k_0$ . At those energies, we find a stronger hydrodynamization signal at the frequency associated with the difference between the energies of the  $n = \pm 2$  and  $\pm 1$  Bragg peaks, which is three times higher than that between the  $n = \pm 1$  and 0 Bragg peaks. The theoretical data in particular, which has better time resolution, ex-

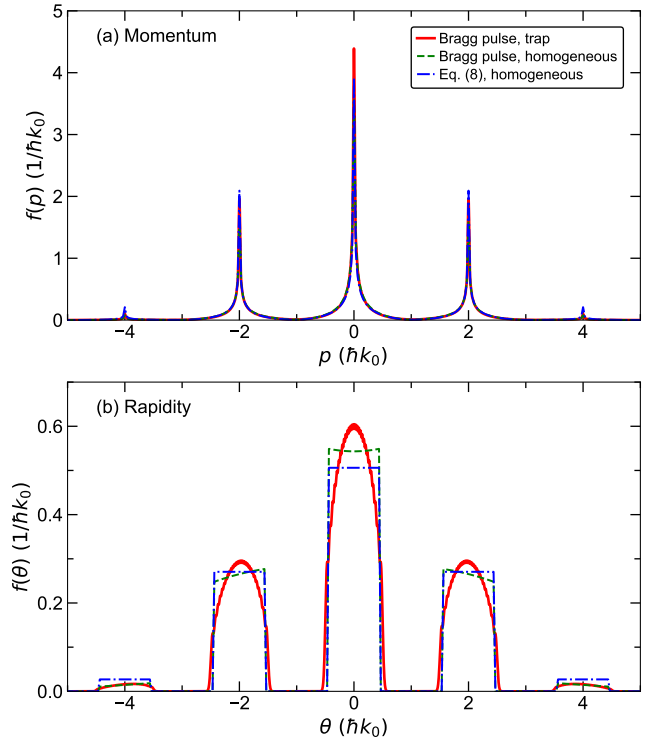


FIG. 7. *Theoretical momentum and rapidity distributions at  $t_{ev} = 0$ .* (a)  $f(p)$  and (b)  $f(\theta)$  for a single TG gas. We show results for a trapped gas after a  $10 \mu s$  Bragg pulse (continuous line), a homogeneous gas after a  $10 \mu s$  Bragg pulse (dashed line), and a homogeneous gas after a Kapitza-Dirac pulse [as per Eq. (8)] with the same area under the pulse as the other two cases (dashed-dotted line). In all three cases, the number of particles is  $N = 29$ , and the energy per particle is the same before the pulse (see text).

hibit clear oscillations of  $E_{\bar{p}}$  with the expected frequency.

There is no QNC pulse sequence that allows us to explore what happens when there are only  $|n| = 1$  peaks. In Sec. V, we solve this problem by directly creating theoretical initial states in which the quasiparticles are in finite superpositions of plane waves with only the  $n = \pm 1$  peaks present, and we study their dynamics under a translationally invariant Hamiltonian.

#### IV. POST-QUENCH STATE MODELING

Equation (8) assumes that the state before the Bragg pulse is the ground state of a homogeneous TG gas, and that the Bragg pulse is infinitely short. In our experiments and their modeling, the initial state is inhomogeneous, because of the trap needed to confine the atoms, and the pulse has a finite duration, because its power is finite. In this section, we explore theoretically the effects of inhomogeneity and finite pulse duration on the dynamics of a single TG gas.

In order to isolate the effects of inhomogeneity, we study the case in which the initial state is the ground

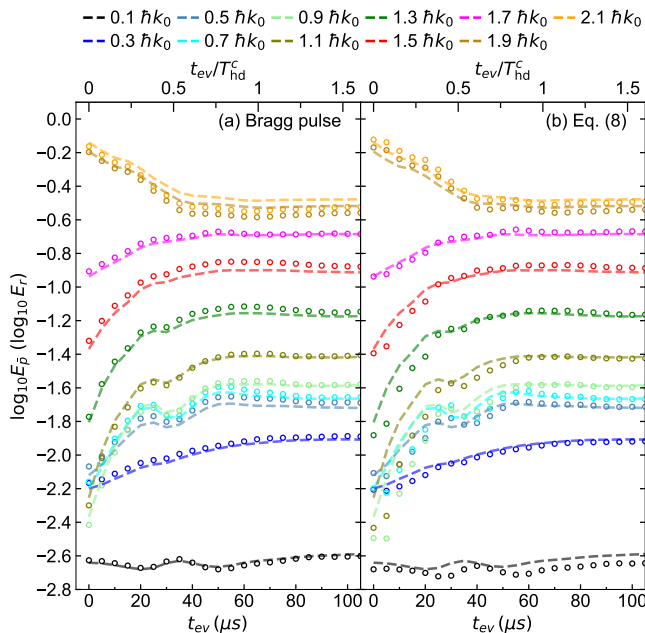


FIG. 8. Time evolution of  $E_{\bar{p}}$  for the homogeneous TG gas. The open symbols show the results after: (a) a  $10 \mu\text{s}$  Bragg pulse, and (b) a Kapitza-Dirac pulse [as per Eq. (8)] with the same area under the pulse as in (a). The dashed lines show the results for the trapped TG gas reported in Fig. 3(b). The number of particles,  $N = 29$ , and the energy per particle before the pulse are the same for the homogeneous TG gas as for the trapped TG gas. To obtain each curve, we integrated within a momentum interval of  $0.2 \hbar k$ . The upper x axis shows the dimensionless quantity  $t_{ev}/T_{hd}^c$  [see Eq. (9)].

state of a homogeneous TG gas with  $N = 29$  particles in a 1D system with periodic boundary conditions [we set  $U(z) = 0$ ], and apply a  $10 \mu\text{s}$  Bragg scattering pulse [Eq. (7)]. We select the same number of particles and apply the same Bragg pulse as in Sec. II B. To most cleanly compare the trapped and homogeneous cases, we choose the size of the homogeneous system so that the energy per particle before the Bragg pulse is the same as in the trapped case. The momentum and rapidity distributions obtained right after the Bragg pulse, for both the trapped and homogeneous case, are plotted in Figs. 7(a) and 7(b), respectively. Away from  $p = \pm 2nk_0$ , for which small differences are seen in Fig. 7(a), the momentum distributions of the trapped and the homogeneous systems are indistinguishable from each other. The corresponding rapidity distributions in Fig. 7(b) are also very close to each other, only differing, as expected, by the fact that in the homogeneous case there are Fermi sea-like discontinuities at the edges of each peak.

To isolate the effects of the finite duration of our Bragg pulse, in Figs. 7(a) and 7(b) we also plot the momentum and rapidity distributions, respectively, for the state predicted by Eq. (8) for a Kapitza-Dirac pulse with the same area as our Bragg pulse applied to the ground state of the homogeneous case. Figure 7(b) shows that the main effect of the finite duration of the Bragg pulse is that

it reduces the transfer of quasiparticles out of the initial Fermi sea, resulting in a slightly lower population of its  $n = \pm 1, \pm 2$  “replicas”. Figure 7(a) shows that this results in slightly lower  $n = \pm 1, \pm 2$  peaks in the momentum distribution after the Bragg pulse. Away from  $p = \pm 2nk_0$ , the momentum distributions are all indistinguishable from each other.

In Fig. 8, we show the evolution of the integrated kinetic energy  $E_{\bar{p}}$  after the Bragg pulse [Fig. 8(a)] and after the Kapitza-Dirac pulse [Fig. 8(b)] for the homogeneous TG gas (empty symbols). Since the two are very similar to each other, it is clear that the finite duration of the pulse, for which there can be many-body evolution during the pulse, does not in fact introduce qualitative changes. In Figs. 8(a) and 8(b) we also show, as thin dashed lines, the results for the trapped system already reported in Fig. 3(b). The evolution in the homogeneous and trapped cases are very similar. In all cases there is a rapid redistribution of kinetic energy, and oscillations of  $E_{\bar{p}}$ , in a time  $T_{hd}^c/2$ . Hence, hydrodynamization, as seen in the experiments and in their corresponding modeling using a trapped TG gas, is qualitatively affected by neither the fact that the system is inhomogeneous nor by the finite duration of the Bragg pulse. Therefore, modeling that directly uses Eq. (8), with the appropriate initial state and area of the Bragg pulse, provides a quantitatively reliable description of the dynamics of the trapped TG gas following the finite-duration Bragg pulse.

Having shown that hydrodynamization is essentially the same in the presence and absence of a trap, as well as with and without finite-time duration pulses, we next explore the local prethermalization of the momentum distribution in the presence and absence of a trap. Local prethermalization refers to the equilibration of the local momentum distribution to the generalized Gibbs ensemble (GGE) prediction [25–28]. During local prethermalization, the overall density distribution does not change significantly. After local prethermalization, trapped systems exhibit global dynamics during which the density distribution changes and with it the local and global rapidity and momentum distributions. Such a long-wavelength and long-time dynamics in an integrable system is described by generalized hydrodynamics (GHD) [29–33], as shown in recent experiments [34–38].

The local prethermalization time for  $f(p)$  is in general momentum-dependent, with the occupation of lower momenta (determined by correlations over longer distances) requiring longer prethermalization times [see Fig. 1(b)]. We will discuss this dependence in more detail in the next section. In the inset in Fig. 9, we plot the time evolution of  $f(p=0)$ , which requires the longest time to prethermalize. We show results following the Bragg pulse in the trapped and homogeneous systems and after the Kapitza-Dirac pulse in the homogeneous system. They all behave qualitatively similarly except at long times. The inset in Fig. 9 shows that after equilibrating to a nearly time-independent value,  $f(p=0)$  in the trapped system departs from that value at  $t \sim 1 \text{ ms}$ . This de-



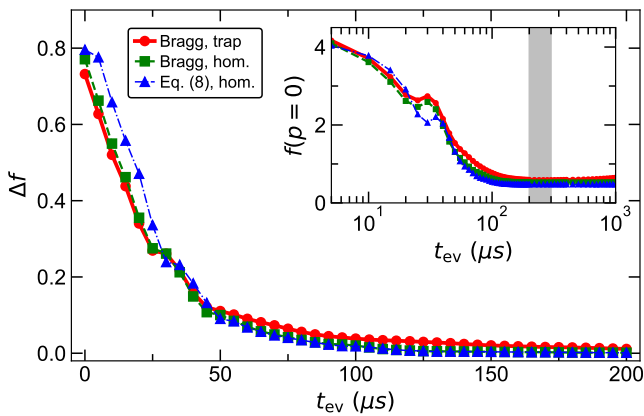


FIG. 9. Time evolution of the momentum distributions of trapped and homogeneous TG gases. Time evolution of  $\Delta f$  [see Eq. (13)] for a trapped gas after a  $10 \mu s$  Bragg pulse (circles), a homogeneous gas after a  $10 \mu s$  Bragg pulse (squares), and a homogeneous gas after a Kapitza-Dirac pulse [as per Eq. (8)] with the same area under the pulse as the other two cases (triangles). In all three cases, the number of particles is  $N = 29$ , and the energy per particle is the same before the pulse. (Inset) Time evolution of  $f(p = 0)$  for the same systems considered in the main panel. The vertical grey band highlights the time interval used to calculate the time-averaged  $\bar{f}(p)$  input in the calculation of  $\Delta f(t_{ev})$ .

parture occurs because the density distribution begins to change in the trap. In the homogeneous cases the density distribution does not change and  $f(p = 0)$  remains unchanged (except for the inevitable revivals that occur in finite systems).

In the inset in Fig. 9 one can see that the values of  $f(p = 0)$  for the three systems considered are nearly time independent in the interval  $t_{ev} \in [200, 300] \mu s$  highlighted by the grey band. We use 6 times spaced by  $\delta t_{ev} = 20 \mu s$  in that interval to calculate the time-averaged momentum distribution  $\bar{f}(p)$ . We take  $\bar{f}(p)$  to be the locally equilibrated momentum distribution. To characterize the local prethermalization of the momentum distribution, we then calculate the relative difference

$$\Delta f(t_{ev}) = \int dp |f(p, t_{ev}) - \bar{f}(p)|. \quad (13)$$

The main panel in Fig. 9 shows the time evolution of  $\Delta f$  for the trapped TG gas after a  $10 \mu s$  Bragg pulse, and for the homogeneous TG gas after a  $10 \mu s$  Bragg pulse and after a Kapitza-Dirac pulse. The three curves are very similar to each other, differing only at the earliest time, presumably because the Bragg pulse calculations get a local prethermalization head start during the pulse. The delay seems unimportant for the characterization of the local prethermalization of  $f(p)$ . As with hydrodynamization, local prethermalization is essentially the same in the presence and absence of a trap, as well as with and without pulses with a finite-time duration.

## V. HYDRODYNAMIZATION AND THE LACK THEREOF IN FINITE SUPERPOSITIONS OF PLANE WAVES

Having shown that there is no need to introduce the trapping potential or to carry out a finite-duration pulse to reproduce the experimental observations, we next take a final step in simplifying our theoretical modeling. In Eq. (8), the quasiparticles are in infinite superpositions of plane waves, corresponding to the infinite Bragg peaks whose weights are determined by the area under the pulse via the Bessel function. In this section, we consider the cases in which only the three or two dominant Bragg peaks from the experiments in Secs. II B and III B, respectively, are present. We study their time evolution under a translationally invariant Hamiltonian.

For all the calculations in this section, we fix the length of our periodic 1D system to be  $L = 20 \times 2\pi/k_0$ , where  $k_0$  is the wavenumber from the experiments discussed in previous sections. To study the effect that changing the particle density (the Fermi momentum  $\theta_F$ ) has on the different time scales, we change the particle number  $N$ .

### A. Three-peak states

We first consider states that have a three-modal rapidity distribution, which we refer to as three-peak states. They have wave functions of the form

$$|\Psi_{3p}\rangle = \prod_{|\theta| < \theta_F} \left( -iA_{-1}\hat{c}_{\theta-2\hbar k}^\dagger + A_0\hat{c}_\theta^\dagger - iA_1\hat{c}_{\theta+2\hbar k}^\dagger \right) |0\rangle, \quad (14)$$

where we have chosen the phases of each “replica” of the initial Fermi sea (with Fermi momentum  $\theta_F$ ) to match those of the Bessel functions in Eq. (8). Choosing other phases introduces phase-shifts with respect to the results in the previous sections, but does not qualitatively change any of the scalings discussed in what follows. We select the weights of the peaks to be  $A_0 = 2/\sqrt{6}$  and  $A_{\pm 1} = 1/\sqrt{6}$ , which are different from the values  $A_0 \approx \sqrt{2}/2$  and  $A_{\pm 1} \approx 1/2$  that we used in Sec. IV when modeling the experiment. As we will see, changing  $A_0$  and  $A_{\pm 1}$  does not qualitatively change the hydrodynamization and prethermalization phenomenology.

In Fig. 10, we plot the time evolution of  $E_{\bar{p}}$  in a homogeneous system with  $N = 33$  bosons with periodic boundary conditions for the three-peak state, showing results for  $k = 3k_0$  [Fig. 10(a)] and  $k = 5k_0$  [Fig. 10(b)]. When plotted in terms of the dimensionless time  $t_{ev}/T_{hd}^c$  (see the upper  $x$  axes labels), the energy curves for different  $k$  exhibit qualitatively similar short-time behavior. For example, the energies  $E_{\bar{p}}$  for  $\bar{p} \sim \hbar k$  initially increase rapidly, and exhibit one period of oscillation, within  $t_{ev} \approx T_{hd}^c/2$ . Those results are qualitatively similar to the ones reported in Fig. 8 although, because  $T_{dp}/T_{hd}^c = \hbar k/(2\theta_F)$  is greater, more hydrodynamization oscillations occur in Fig. 10 for  $p \approx \hbar k$ . The hy-

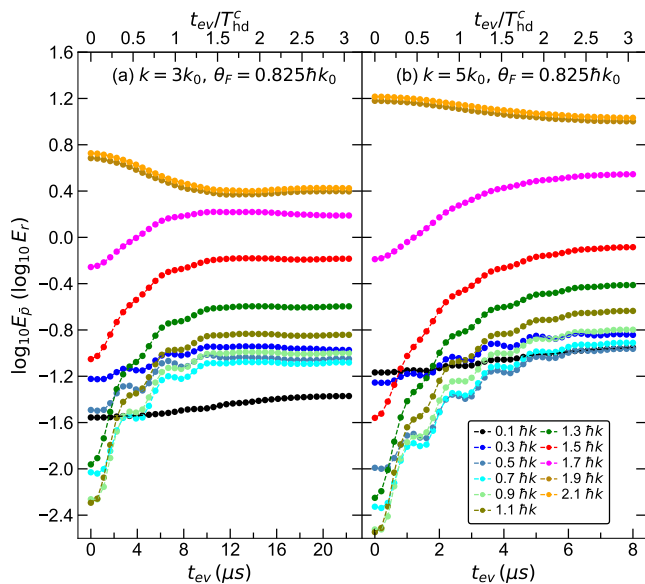


FIG. 10. Time evolution of  $E_{\bar{p}}$  for three-peak states [see Eq. (14)] with  $A_0 = 2/\sqrt{6}$  and  $A_{\pm 1} = 1/\sqrt{6}$ . We show results for systems with  $N = 33$  ( $\theta_F = 0.825\hbar k_0$ ) for (a)  $k = 3k_0$  and (b)  $k = 5k_0$ . Each curve is integrated within a  $0.2 \hbar k$  momentum interval. Note that the time axes differ in the two panels. The upper  $x$  axis shows the dimensionless quantity  $t_{ev}/T_{hd}^c$ .

drodynamization oscillation period does not significantly depend on  $p$ , but the hydrodynamization damping times and the local prethermalization times do depend on  $p$ .

Next, we study the prethermalization of the momentum distribution in more detail. As shown in Refs. [25, 39, 40], the integrability of the Tonks-Girardeau gas implies that the momentum distribution after equilibration is not thermal. Instead, it is described by a GGE that is fully determined by the conserved rapidity distribution of the underlying quasiparticles. Similar re-

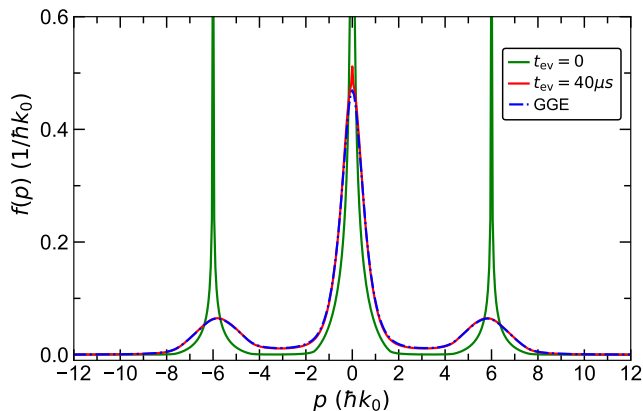


FIG. 11. Evolution of the momentum distribution  $f(p)$  for a three-peak state. The solid lines show  $f(p)$  at  $t_{ev} = 0$  (green) and  $40 \mu s$  (red) for the same initial state as in Fig. 10(a). The blue dashed line shows the GGE prediction.

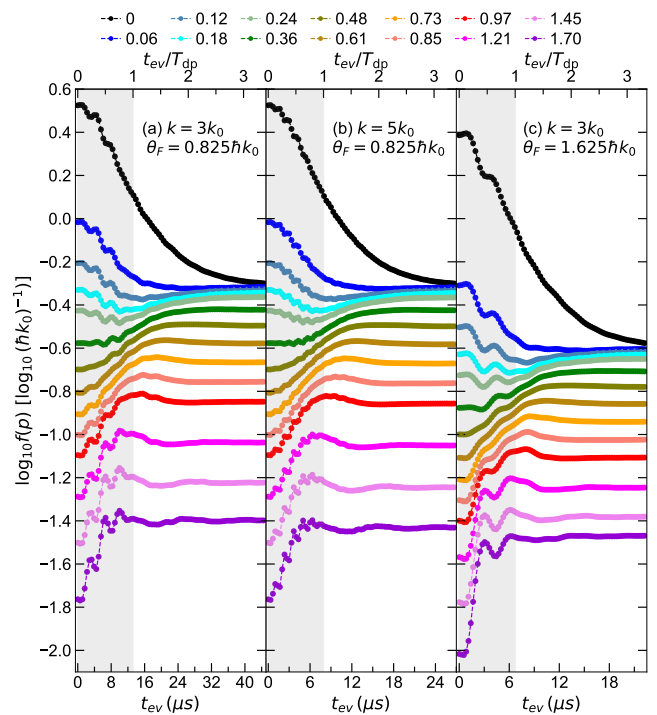


FIG. 12. Time evolution of  $f(p)$  within the central peak for three-peak states. The initial states have: (a)  $N = 33$  ( $\theta_F = 0.825\hbar k_0$ ) and  $k = 3k_0$ , (b)  $N = 33$  ( $\theta_F = 0.825\hbar k_0$ ) and  $k = 5k_0$ , and (c)  $N = 65$  ( $\theta_F = 1.625\hbar k_0$ ) and  $k = 3k_0$ . Note the change in the times shown in each panel. The upper  $x$  axis shows the dimensionless quantity  $t_{ev}/T_{dp}$ . The legends show the value of  $p/\theta_F$ . The vertical grey bands ( $t_{ev} \in [0, 1]T_{dp}$ ) highlight the time scale in which the hydrodynamization oscillations damp out.

sults have been obtained in other paradigmatic integrable models that map onto quadratic ones, such as the Luttinger model [41] and the transverse-field Ising model in 1D [27, 42, 43]. In Fig. 11, we show  $f(p)$  for the state studied in Fig. 10(a) at  $t_{ev} = 0$  and  $40 \mu s$ , along with the GGE prediction. Except for the occupation of  $p = 0$ , which requires a longer time to equilibrate,  $f(p)$  at  $t_{ev} = 40 \mu s$  is indistinguishable from the GGE prediction.

How the occupation  $f(p)$  of each momentum mode approaches the GGE prediction depends in a complicated way on  $p$ ,  $k$ , and  $\theta_F$ . In Fig. 12, we show the time evolution of  $f(p)$  for  $p < 2\theta_F$  (i.e., within the central momentum peak), for  $N = 33$  when  $k = 3k_0$  [Fig. 12(a)] and when  $k = 5k_0$  [Fig. 12(b)], and for  $N = 65$  when  $k = 3k_0$  [Fig. 12(c)]. Note that the absolute time axes differ across the panels so that the dimensionless (upper) time axes  $t_{ev}/T_{dp}$  [see Eq. (18)] are the same. The results in Fig. 12 show that, for any given pair of values of  $k$  and  $\theta_F$ , the shapes of the  $f(p)$  vs  $t_{ev}$  curves change when changing  $p$ , with the prethermalization time increasing as  $p$  approaches 0. Fixing  $p/\theta_F$  (which have the values reported in the legends) and changing  $k$  or  $N$  also results in changes in the  $f(p)$  curves. There are, however, two universal features that can be seen across Figs. 12(a)–

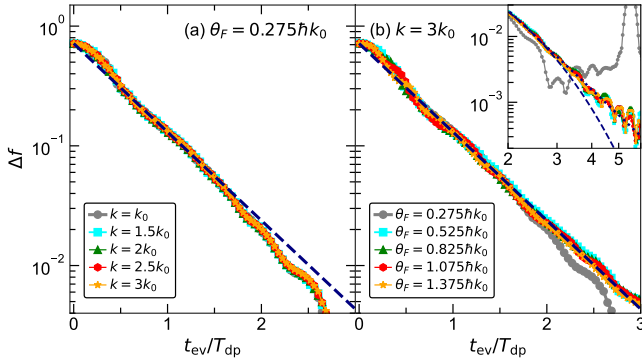


FIG. 13. *Prethermalization of  $f(p)$  for three-peak states.*  $\Delta f$  vs the dimensionless time  $t_{\text{ev}}/T_{\text{dp}}$ . (a) We fix  $N = 11$  ( $\theta_F = 0.275\hbar k_0$ ) and show results for different  $k$ . (b) We fix  $k = 3k_0$  and show results for different  $N$  ( $\theta_F$ ). The dashed lines show the result of a fit  $a \exp(-b t_{\text{ev}}/T_{\text{dp}})$  to the results for the largest number of particles in (b), which yields  $b = 1.7$ . Inset of (b): same as (b) but plotted on a log-log scale for later times. The dashed line is the same exponential fit as in the main panels. The dotted line is a power law guide to the eye,  $(t_{\text{ev}}/T_{\text{dp}})^{-4}$ . The  $N = 11$  ( $\theta_F = 0.275\hbar k_0$ ) curve exhibits a revival after  $t_{\text{ev}} = 5T_{\text{dp}}$ , a finite size effect resulting from the small number of particles.

12(c). The first is that the damping of the hydrodynamization oscillations in all panels and for all  $p$  occurs within  $t_{\text{ev}} \simeq T_{\text{dp}}$  (highlighted by the shaded bands). The second is that the prethermalization time for  $f(p)$ , i.e., the time after which the  $f(p)$  curves become nearly time independent, are momentum independent when  $p \gtrsim \theta_F$ .

The diversity of shapes among the  $f(p)$  curves in Fig. 12 make it clear that defining the prethermalization time for different momentum modes  $p$  is a challenging task, even if one were to smooth out the hydrodynamization oscillation. Addressing this challenge is postponed to future work. The results in Fig. 12 also hint that the prethermalization times for all momentum modes are proportional to  $T_{\text{dp}}$ , because one can see that for each value of  $p/\theta_F$ , equilibration in different panels occurs at about the same value of  $t_{\text{ev}}/T_{\text{dp}}$ . Building on this observation, we next show that the prethermalization time scale for the entire momentum distribution is indeed proportional to  $T_{\text{dp}}$ .

In Fig. 13, we plot the time evolution of  $\Delta f$  [see Eq. (13)] vs  $t_{\text{ev}}/T_{\text{dp}}$  for systems with the same number of particles ( $N = 11$ ) and different  $k$  [Fig. 13(a)], and for systems with the same value of  $k = 3k_0$  and different  $N$  [Fig. 13(b)]. In both panels, one can see that the curves of  $\Delta f$  vs  $t_{\text{ev}}/T_{\text{dp}}$  collapse onto each other, except for the  $N = 11$  curve past  $t_{\text{ev}} \sim 1.5T_{\text{dp}}$  in Fig. 13(b), which deviates due to finite-size effects. For times  $0.5T_{\text{dp}} \lesssim t_{\text{ev}} \lesssim 3T_{\text{dp}}$ , the results for  $N > 11$  are well described by an exponential function. Specifically,  $\Delta f(t) \propto \exp(-b t_{\text{ev}}/T_{\text{dp}})$ , which means that the prethermalization time  $T_{\text{lp}}$  for the momentum distribution is proportional to  $T_{\text{dp}}$ . [Once  $\Delta f(t)$  becomes a fraction of a percent near  $t_{\text{ev}} \sim 3T_{\text{dp}}$ , the evolution slows down, tran-

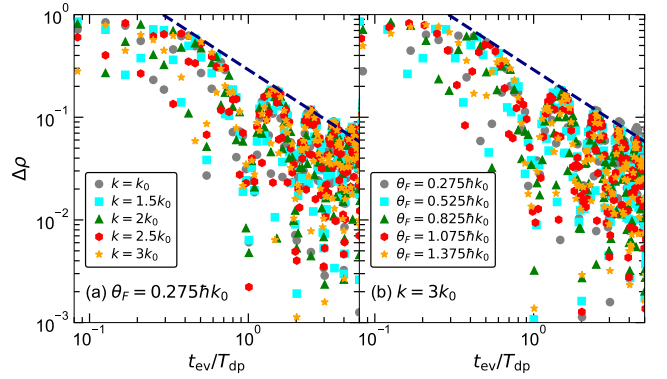


FIG. 14. *Prethermalization of  $\rho(z)$  for three-peak states.* Same as Fig. 13 but for  $\Delta\rho$  [see Eq. (15)]. The dashed lines, which are guides to the eye, show  $(t_{\text{ev}}/T_{\text{dp}})^{-1}$  behavior.

sitioning to a roughly polynomial decay in time (see the inset in Fig. 13(b). Since the effect may be too small to experimentally detect, we will not explore it further here.) It has previously been argued that the quantum dynamics of TG gas momentum distributions can be like those of generic observables in interacting integrable models that cannot be mapped onto noninteracting models [44]. We therefore expect our TG results to qualitatively describe dynamics away from the TG limit, where the Lieb-Liniger model cannot be mapped onto a noninteracting model, with a proportionality constant between  $T_{\text{lp}}$  and  $T_{\text{dp}}$  that depends on the contact interaction strength  $g$ .

In contrast, we do not expect the TG gas to serve as a model for the quantum dynamics of the density distribution in the experiments. That is because the matrix elements of few-body observables in noninteracting models are qualitatively different from those in interacting models [44]. The density dynamics of a TG gas and a noninteracting Fermi gas are identical, while there is no such mapping for a Lieb-Liniger gas away from the TG limit. The Gaussian nature of the energy eigenstates in noninteracting models makes the observables equilibrate polynomially in time [45–49], as opposed to exponentially.

In Fig. 14, we plot the time evolution of the normalized integrated difference between the density distribution of our TG gases at different evolution times and the constant density  $N/L$  achieved after prethermalization

$$\Delta\rho(t_{\text{ev}}) = \frac{1}{N} \int dz \left| \rho(z, t_{\text{ev}}) - \frac{N}{L} \right| \quad (15)$$

vs  $t_{\text{ev}}/T_{\text{dp}}$ . Results for  $\Delta\rho(t_{\text{ev}})$  are shown for systems with the same number of particles ( $N = 11$ ) and different  $k$  [Fig. 14(a)], and for systems with the same value of  $k = 3k_0$  and different  $N$  [Fig. 14(b)], which parallel the results for  $\Delta f(t_{\text{ev}})$  in Figs. 13(a) and 13(b), respectively. In contrast to  $\Delta f(t_{\text{ev}})$ ,  $\Delta\rho(t_{\text{ev}})$  exhibits large fast changes on the hydrodynamization time scale, the result of the oscillations of  $\rho(z, t_{\text{ev}})$  discussed earlier (and shown in Fig. 1c of Ref. [5]). There are also oscillations with

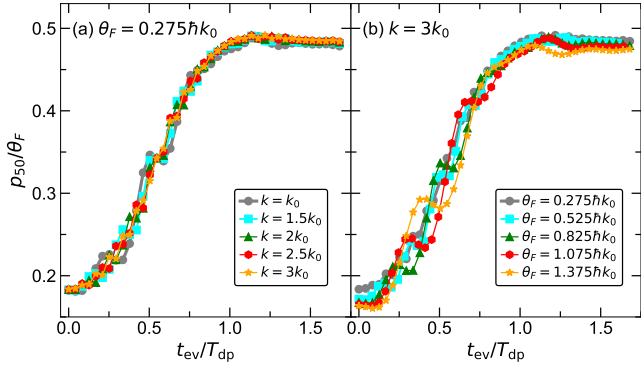


FIG. 15. *Prethermalization of  $p_{50}$  for three-peak states.*  $p_{50}/\theta_F$  vs the dimensionless time  $t_{ev}/T_{dp}$ . (a) We fix  $N = 11$  ( $\theta_F = 0.275\hbar k_0$ ) and show results for different  $k$ . (b) We fix  $k = 3k_0$  and show results for different  $N$  ( $\theta_F$ ).

the longer  $T_{dp}$  period. Most notably and as expected, the amplitude of the oscillations decays polynomially (as opposed to exponentially) in time as  $(t_{ev}/T_{dp})^{-1}$ , as demarcated by the dashed lines in the plots. We expect this decay to change into an exponential decay as one moves away from the TG limit, a change that could be explored in future studies.

We close our discussion of the three-peak case by connecting our results for prethermalization here to the local prethermalization results reported in Ref. [5]. There we studied the time evolution of “ $p_f$ ”, which is defined so that  $\pm p_f$  are the momenta enclosing  $f\%$  of the atoms in the central peak. Since the results were found to be qualitatively similar for  $f$  in the range of 40 to 60, we focused on  $f = 50$ ,

$$\int_{-p_{50}}^{p_{50}} f(p) dp = \frac{A}{2}, \quad (16)$$

where  $A$  is the area of the central peak.

In Fig. 15, we plot the theoretical time evolution of  $p_{50}/\theta_F$  vs  $t_{ev}/T_{dp}$  for three-peak states with the same number of particles ( $N = 11$ ) when we change  $k$  [Fig. 15(a)], and with the same value of  $k = 3k_0$  when we change the number of particles [Fig. 15(b)]. The curves collapse onto each other. That is, the prethermalization time for  $p_{50}$  is proportional  $T_{dp}$ . It is remarkable that the same holds true for the experimental results reported in Ref. [5], for which the contact interaction strength  $g$  had a finite constant value and the 1D density was changed to change the width of the rapidity distribution. While the local prethermalization time was found to be about three times longer in the experiments than in the TG theory, its scaling with  $T_{dp}$  was the same. Those results suggest that the proportionality constant between the local prethermalization time and  $T_{dp}$  depends on  $g$  [see Eq. (1)] and not on the density (or  $\theta_F$ ). This is unlike the thermal equilibrium properties of the Lieb-Liniger gas, which are fully determined by  $\gamma$ .

## B. Two-peak states

Next, we study the dynamics after removing the central peak, so that we have bimodal rapidity distributions with  $A_{\pm 1} = 1/\sqrt{2}$ :

$$|\Psi_{2p}(t_{ev} = 0)\rangle = \prod_{|\theta| < \theta_F} \frac{1}{\sqrt{2}} (\hat{c}_{\theta+2\hbar k}^\dagger + \hat{c}_{\theta-2\hbar k}^\dagger) |0\rangle. \quad (17)$$

There is no hydrodynamization time scale associated with these “two-peak” states. Dephasing of rapidities still occurs, leading to evolution of observables, but it can all be characterized as local prethermalization. Dephasing results from the energy differences between the quasiparticles with rapidities  $\theta - 2\hbar k$  and  $\theta + 2\hbar k$ , which have different values within a bandwidth  $W'$ , which is twice as large as in the three-peak case  $W' = 2W = 16\hbar k \theta_F / (2m)$ . The dephasing time scale is thus twice as fast for any given  $k$  and  $\theta_F$

$$T'_{dp} = \frac{2\pi\hbar}{W'} = \frac{\pi m}{4k\theta_F}. \quad (18)$$

In Fig. 16, we plot the time evolution of  $E_{\bar{p}}$  for two-peak states for two values of  $k$ , as we did in Fig. 10 for three-peak states. There are no hydrodynamization oscillations, as was also illustrated in the QNC pulse states of Sec. III B (except for the complication of residual extra peaks). All one can see in Fig. 16 is local prethermalization, which occurs in a time that is proportional to  $T'_{dp}$  (see the top  $x$  axis scale). These results highlight the importance of having a multimodal energy distribution for

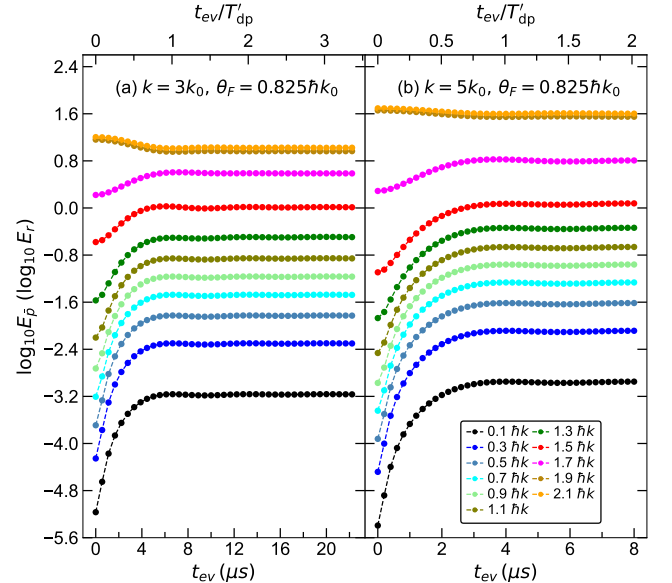


FIG. 16. *Time evolution of  $E_{\bar{p}}$  for the “two-peak state”* [see Eq. (17)]. We show results for a system with  $N = 33$  atoms ( $\theta_F = 0.825$ ) for (a)  $k = 3k_0$  and (b)  $k = 5k_0$ . Each curve is integrated within a momentum interval of  $0.2 \hbar k$ . Note the change in the times shown in both panels. The upper  $x$  axis shows the dimensionless quantity  $t_{ev}/T'_{dp}$ .



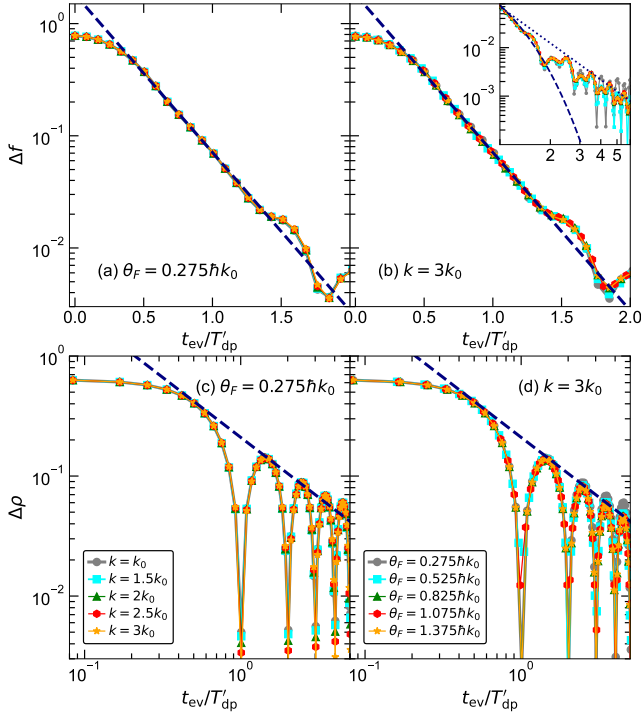


FIG. 17. *Local prethermalization of  $f(p)$  and  $\rho(z)$  for the “two-peak” state.* (a) and (b)  $\Delta f$  vs the dimensionless time  $t_{\text{ev}}/T'_{\text{dp}}$ .  $N$  and  $k$  for simulation are the same as the ones in Fig. 13. The dashed lines show a fit  $a \exp(-bt_{\text{ev}}/T'_{\text{dp}})$  to the results with largest atom number in (b) and  $t_{\text{ev}} \in (0.5, 1.5)T'_{\text{dp}}$ , which yields  $b = 3.2$ . Inset of (b): same as (b) but plotted on a log-log scale for later times. The dashed line is the same exponential fit as in (b). The dashed line is a guide to the eye and shows power law behavior,  $(t_{\text{ev}}/T'_{\text{dp}})^{-2.5}$ . (c)[(d)] Same as (a) [(b)], but for  $\Delta\rho$ . The dashed lines show  $(t_{\text{ev}}/T'_{\text{dp}})^{-1}$  behavior as in Fig. 14.

hydrodynamization to occur. They also highlight that local prethermalization can occur in remarkably short times even in the absence of hydrodynamization, because the local prethermalization time is inversely proportional to  $k$ , which is not related to any microscopic scale associated with the Hamiltonian of the many-body system.

In Fig. 17 we report our results for two-peak states for  $\Delta f$  vs  $t_{\text{ev}}/T'_{\text{dp}}$  [Figs. 17(a) and 17(b)] and for  $\Delta\rho$  vs  $t_{\text{ev}}/T'_{\text{dp}}$  [Figs. 17(c) and 17(d)]. They parallel the results for the same quantities for three-peak states shown in Figs. 13 and 14, respectively. All the features discussed about the prethermalization of the momentum and density distributions of the three-peak states are apparent in the two peak case. There are two main differences. First, the hydrodynamization oscillations of the density, which can be seen in Fig. 14, are not present in Figs. 17(c) and 17(d) (the only oscillations present in Figs. 17(c) and 17(d) are the ones with a period  $T'_{\text{dp}}$ ). Second, the prefactor  $b$  of the dimensionless time in the exponential decay of  $\Delta f$  in Figs. 17(a) and 17(b) is about twice that in Fig. 13, while the dimensionless time during which this exponential decay is visible in Figs. 17(a) and 17(b) is

about half what it is in Fig. 13. In both systems, a slower power-law decay in time seems to emerge at late times when  $\Delta f$  is smaller than a fraction of a percent. Given the smallness of  $\Delta f$  at those times, such a slower decay is probably irrelevant to experimental observations, but it might be of interest to explore theoretically in the future.

### C. Symmetric two-peak states

The contrast between our three and two peak results makes it clear that the time evolution of observables depends crucially on the rapidity distributions. The Bohr factors also matter greatly. To illustrate this point, we constructed the following many-quasiparticle states

$$|\Psi_e\rangle = \prod_{|\theta| < \theta_F} \frac{1}{\sqrt{2}} (\hat{c}_{\theta+2\hbar k}^\dagger + \hat{c}_{-\theta-2\hbar k}^\dagger) |0\rangle. \quad (19)$$

They have the same rapidity distribution as the states in Eq. (17), yet because each term in the product state consists of a superposition of equal energy states, such symmetric two-peak states exhibit no dynamics; they are eigenstates of the translationally invariant TG gas. Also, despite having the same rapidity distributions, the states

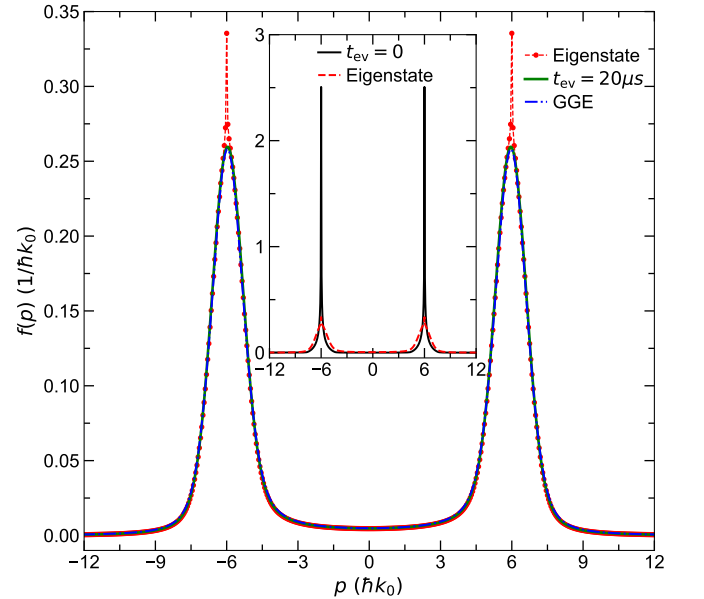


FIG. 18. *Momentum distributions for two-peak states.* Main panel:  $f(p)$  for the two-peak post-quench wave function [Eq. (17), with  $k = 3k_0$  and  $N = 33$ ] at  $t_{\text{ev}} = 20 \mu\text{s}$  (green solid line), the corresponding symmetric two-peak state [Eq. (19)] (red dashed line), and the GGE prediction (blue dashed-dotted line). Inset:  $f(p)$  for the two-peak post-quench wave function [Eq. (17), with  $k = 3k_0$  and  $N = 33$ ] at  $t_{\text{ev}} = 0 \mu\text{s}$  (black solid line) and the corresponding symmetric two-peak state [Eq. (19)] (red dashed line). The small red dots in the main panel mark the quantized momenta in our finite system.

in Eqs. (17) and (19) have different momentum distributions, as shown in the inset in Fig. 18.

Because of generalized eigenstate thermalization [27, 50–54], the momentum distribution of the state in Eq. (17) is expected to equilibrate to the same momentum distribution as all energy eigenstates that have the same rapidity distribution, to within differences that vanish in the thermodynamic limit. Our results in Fig. 18 confirm this. The asymptotic  $f(p)$  (at  $t_{ev} = 20 \mu s$ ) from the superposition of Eq. (17) exactly coincides with the GGE prediction. The unchanging momentum distribution from the symmetric two-peak state [Eq. (19)] is also indistinguishable from the GGE prediction at all momenta, except for at the singular  $|p| = 2\hbar k$  point and the nearest momentum points to it. As in many other systems studied in the literature (see Ref. [27] for a review), we expect the normalized differences between the equilibrated, the GGE, and the symmetric two-peak state momentum distributions, which are small but finite in our finite systems, to vanish in the thermodynamic limit.

## VI. HEAVY ION COLLISIONS

We next apply the lessons we have learned about hydrodynamization and local prethermalization to relativistic heavy ion collisions. To avoid confusion in the application of these ideas to particles physics, it is important to make clear that the term “rapidities” used in this paper and in the integrable systems literature (denoting the momenta of quasiparticles) has no relation to rapidities in high energy physics (denoting transverse relativistic momenta). The two and three peak quenches of 1D gases that we consider in this paper resemble collisions between atomic groups with distinct momenta, with the provisos that each single atom’s wave function is part of all colliding groups and there is significant entanglement among individual atoms. The fact that the “colliding” parts of the wave function spatially overlap from the very beginning of the quench is critical to their value in understanding short-time evolution. The short-time behavior would be difficult to extract in a conventional collision between incident clouds of atoms, as it would happen throughout the process of the clouds spatially merging.

It will become apparent below that the time it takes for colliding relativistic nuclei to overlap is generally shorter than the time it takes for hydrodynamization to run its course. To estimate the time it takes for the nuclei to overlap, note that the highest collision energies probed at the Relativistic Heavy Ion Collider (RHIC) and the Large Hadron Collider (LHC) have  $\gamma_L = 1/\sqrt{1 - v^2/c^2}$  Lorentz factors of about 100 and 2500, respectively. In the lab frame, the nuclei look like space contracted disks of  $D/\gamma_L$ , where  $D$  is the nuclear diameter ( $D \sim 14$  fm for heavy nuclei), traveling at about the speed of light,  $c$ . The two nuclei are fully overlapped in a head-on collision within  $\simeq 0.14$  fm/ $c$  at RHIC and  $\simeq 0.0056$  fm/ $c$  at the LHC. We take the point of full overlap as  $t = 0$  for con-

sidering post-quench evolution, analogous to the time at the end of a Bragg-pulse quench of 1D gases.

The colliding nuclei form a quark-gluon plasma, which grows as the nuclei recede from each other. The system is far from integrable, so its large-distance and long-time dynamics are described by hydrodynamics with a very small ratio between the shear viscosity  $\eta$  and the entropy density  $s$ ,  $\eta/s \approx 1/(4\pi)$ . ( $\eta/s = 1/(4\pi)$  is the ratio found in infinitely strongly coupled quantum theories described by a holographic dual gravitation theory [55].) This small ratio implies that the quark-gluon plasma is a strongly coupled fluid, unlike the asymptotically free quarks and gluons at much higher energies [9]. That is, the quark-gluon plasma is an interacting many-body quantum system, amenable to the approach to studying dynamics we use in this paper. A major open question in the description of heavy-ion collisions is why hydrodynamics works at very short times after the collision. The proper times  $\tau_0^{\text{exp}}$  at which hydrodynamic descriptions start to work depend on the specific model used in calculations; they are around 0.4–1.0 fm/ $c$  for the RHIC and 0.2–0.6 fm/ $c$  for the LHC [9]. Our goal here is to provide insight into this open question.

We assume that there is a quasiparticle description of the quark-gluon plasma. Although the quark-gluon plasma is not integrable, these quasiparticles do not decay on hydrodynamization time scales, since they are the fastest time scales in the many-body system. We label the quasiparticle masses  $m_{qs}$ . Although these masses are unknown, we assume that they are smaller than the *constituent quark* masses of the  $u$  and  $d$  quarks ( $\sim 300$  MeV/ $c^2$ ) and larger than the *current quark* masses ( $\sim 3$  MeV/ $c^2$ ). The two orders of magnitude difference between *current quark* and *constituent quark* masses are due to the gluon field [56, 57]. The rapidity distribution is also unknown, but if there has not been enough time for significant many-body evolution, then the longitudinal rapidity distribution will contain peaks at  $\pm\theta_{\gamma_L} = \pm\gamma_L m_{qs} c$ , corresponding to the incoming nuclei. Using the uncertainty principle in the lab frame, we can bound the widths of these rapidity distribution peaks to be  $\Delta\theta_{\gamma_L} \geq \hbar\gamma_L/(2D)$ . In the limit of  $\gamma_L \gg 1$ , the energy of a quasiparticle with rapidity  $\simeq \pm\theta_{\gamma_L}$  is  $E \simeq \theta_{\gamma_L} c$ .

The initial stage of the heavy-ion collision in the lab frame can be viewed as a continuous process that transfers quasiparticles from  $\theta \simeq \pm\theta_{\gamma_L}$  to the  $t = 0$  rapidity distribution of the quark-gluon plasma, analogous to the 1D gas Bragg pulse continuously transferring amplitude to the side rapidity peaks. It seems likely that this initial rapidity distribution contains a peak of similar width to the side peaks at rest in the lab frame. As in a 1D gas right after a Bragg quench, some hydrodynamization and/or local prethermalization may occur while the starting time is approached, but it is not qualitatively important.

After  $t = 0$ , we can apply the same explanation we used for hydrodynamization in 1D gases to the evolution of the momentum distribution, which contains all

the information about the relative amplitudes of the partons (quarks, antiquarks, and gluons). As in 1D gases, the momentum distribution of the partons in the quark-gluon plasma will exhibit hydrodynamization oscillations on a time scale  $\tau_{\text{hd}}^c = 2\pi\hbar/(\theta_{\gamma_L}c)$ .  $\tau_{\text{hd}}^c$  depends on the unknown mass of the quasiparticles and on  $\gamma_L$ . Given our assumption about the quasiparticle masses,  $\tau_{\text{hd}}^c$  is bounded by 0.04 (0.002) and 4 (0.2) fm/c for the RHIC (LHC) experiments. If one were able to experimentally or numerically probe such oscillations, as we have done for TG gases, one could determine  $m_{\text{qs}}$  using  $\tau_{\text{hd}}^c$ .

The damping of these hydrodynamization oscillations occurs within a time  $\tau_{\text{hd}}^d$ . Notably, this time depends on the widths of the rapidity distribution peaks, but not on the unknown masses of the quasiparticles. Given our bound for the width of these peaks, we expect  $\tau_{\text{hd}}^d \leq 2\pi D/(\gamma_L c)$ . As in our 1D gases, we anticipate the shortest local *prethermalization* time for the momentum distribution of partons with high momenta to be of the same order as  $\tau_{\text{hd}}^d$ . Although the quark-gluon plasma ultimately *thermalizes* locally, *prethermalization* is the appropriate concept here for times short enough that bare particles cannot traverse their interparticle separation. At longer times, there will be local thermalization and the associated decay of quasiparticles.

Assuming minimal uncertainty and using the largest values of  $\gamma_L$  from each experiment,  $\tau_{\text{hd}}^d \simeq 0.9$  fm/c for the RHIC and  $\tau_{\text{hd}}^d \simeq 0.04$  fm/c for the LHC. These values would decrease if  $\Delta\theta_{\gamma_L}$  is in fact larger than our uncertainty principle-limited lower bound, and would increase if we decrease  $\gamma_L$ . These times are generally in the range of or somewhat shorter than the times after which hydrodynamics starts to describe the quark-gluon plasma (recall, 0.4–1.0 fm/c for the RHIC and 0.2–0.6 fm/c for the LHC [9]). Hydrodynamics cannot be used to describe dynamics until after hydrodynamization has run its course in  $\sim \tau_{\text{hd}}^d$ . Until then, there are significant short distance spatial fluctuations and bare particle energies are still being redistributed across distant momentum modes.

Therefore, the earliest time for which hydrodynamics can possibly work is  $\sim \tau_{\text{hd}}^d$ . But how soon after  $\tau_{\text{hd}}^d$  hydrodynamics becomes a reliable description is a subtle question. That it might be roughly coincident with  $\tau_{\text{hd}}^d$  is supported by our study of 1D gases, where we have shown that  $T_{\text{hd}}^d$  scales the same as  $T_{\text{dp}}$ , and the normalized difference between the time-evolving  $f(p)$  and the local prethermalized  $f(p)$  decreases from  $\sim 10\%$  to  $\sim 1\%$  between  $T_{\text{dp}}$  and  $2T_{\text{dp}}$  (see Fig. 13). Furthermore, in multiple studies of integrable models after quantum quenches, it has been found that observables after local prethermalization can be very close to locally thermal [28] (see, e.g., Ref. [58] for a systematic study of a specific family of initial states). Putting these two sets of observations together, if on the  $T_{\text{dp}}$  timescale  $f(p)$  in the quark-gluon plasma approaches the locally prethermalized state and the locally prethermalized  $f(p)$  is similar to  $f(p)$  after local thermalization, hydrodynamics should be reasonably accurate soon after  $\sim \tau_{\text{hd}}^d$ . We note that

in the special case of Bragg-scattered near-integrable 1D Bose gases, generalized hydrodynamics demonstrably applies for times  $\gtrsim T_{\text{hd}}^d$  [5]. If it turns out that  $\tau_0^{\text{exp}}$  is somewhat bigger than  $\tau_{\text{hd}}^d$ , then there would be a minor nomenclature discrepancy, in that our usage of hydrodynamization would not coincide with the applicability of hydrodynamics, as in the original high-energy coining of the term.

As an additional note, if the collision between the heavy nuclei does not produce a quasiparticle peak about  $\theta = 0$ , but instead simply entangles the quasiparticles with rapidities about the  $\theta_{\gamma_L}$  peak with those about the  $-\theta_{\gamma_L}$  peak, then hydrodynamization oscillations would not occur (as discussed for the two peak case in Sec. VB). Local prethermalization would still occur with the same scaling with  $\tau_{\text{hd}}^d$  discussed above, assuming that all quasiparticles from one peak are entangled with all the quasiparticles from the other peak. Thus either of the two scenarios discussed in Secs. VA and VB, for three and two peaks in the rapidity distributions, respectively, are consistent with the short times for which hydrodynamics can be used to describe the experimental results.

## VII. SUMMARY

Our results show that in high-energy quenches involving multimodal rapidity distributions, hydrodynamization and local prethermalization dynamics proceed on remarkably short time scales. These time scales are set by the amount of energy put in the system via the quench. Assuming that even nonintegrable systems have well defined (albeit typically hard to calculate) quasiparticles on such short time scales, we have qualitatively explained why hydrodynamics works so soon after the start of a heavy-ion collision.

The quasiparticle description of an interacting many-body system after a quench depends on the relevant detailed physics. However, the subsequent dynamics is rather universal. If there are three peaks in the rapidity distribution (the momentum distribution of the quasiparticles) then observables will exhibit hydrodynamization oscillations characterized by the time  $T_{\text{hd}}^c$ . These oscillations damp out on the  $T_{\text{hd}}^d$  time scale, where the particular damping coefficient depends on the observable. The highest momentum components of the momentum distribution start to locally prethermalize in a time  $T_{\text{p}}$ , which is equal to or greater than  $T_{\text{hd}}^d$ . Hydrodynamization and initial local prethermalization are dominated by spatial changes on distance scales shorter than interparticle separations and by exchanges of energy among disparate energy modes. All of these dynamics are fundamentally quantum mechanical in nature, a consequence of Bohr factors in the many-body wavefunction, with non-integrable analogue.

The dynamics of subsequent local prethermalization, which will generally overlap with local thermalization in non-integrable systems, is also contained in the Bohr fac-

tors of many-body wavefunctions. But unlike the initial evolution, spatial changes occur on distances greater than interparticle separations and energy is exchanged primarily among nearby modes. Such processes more readily lend themselves to semi-classical pictures. We have further shown in this paper that for situations where there are only two peaks in the rapidity distribution, there are no hydrodynamization oscillations, even when the quench energy is the same as in a three-peak quench. In that case, the fastest prethermalization evolution still scales with  $T_{\text{hd}}^d$ , as in the three-peak case.

For future studies with 1D gases, we envision exploring what happens as one controllably breaks integrability, as was done, e.g., in Ref. [14] for a QNC sequence. It appears particularly interesting to understand how the nature of the state at times  $\sim T_{\text{hd}}^d$  changes, as well as the interplay between local prethermalization and local

thermalization, as one departs from the near-integrable regime. Beyond 1D gases, Bragg scattering quenches in unitary 3D gases [59, 60] may be good candidates for directly studying the interplay between local prethermalization and local thermalization in far from integrable systems.

## ACKNOWLEDGMENTS

We thank Sarang Gopalakrishnan for discussions early in this work. Y.Z. acknowledges support from the Dodge Family Postdoc Fellowship at the University of Oklahoma. M.R. acknowledges support from the National Science Foundation under Grant No. PHY-2309146. D.S.W. and Y.L. acknowledge support from the National Science Foundation under Grant No. PHY-2012039.

- 
- [1] J. J. Sakurai and J. Napolitano, *Modern Quantum Mechanics* (Cambridge Univ. Press, Cambridge, 2020).
  - [2] V. E. Korepin, N. M. Bogoliubov, and A. G. Izergin, *Quantum Inverse Scattering Method and Correlation Functions* (Cambridge Univ. Press, Cambridge, 1993).
  - [3] J. M. Wilson, N. Malvania, Y. Le, Y. Zhang, M. Rigol, and D. S. Weiss, Observation of dynamical fermionization, *Science* **367**, 1461 (2020).
  - [4] K.-Y. Li, Y. Zhang, K. Yang, K.-Y. Lin, S. Gopalakrishnan, M. Rigol, and B. L. Lev, Rapidity and momentum distributions of one-dimensional dipolar quantum gases, *Phys. Rev. A* **107**, L061302 (2023).
  - [5] Y. Le, Y. Zhang, S. Gopalakrishnan, M. Rigol, and D. S. Weiss, Observation of hydrodynamization and local prethermalization in 1D Bose gases, *Nature* **618**, 494 (2023).
  - [6] J. Berges, S. Borsányi, and C. Wetterich, Prethermalization, *Phys. Rev. Lett.* **93**, 142002 (2004).
  - [7] M. P. Heller and M. Spaliński, Hydrodynamics beyond the gradient expansion: Resurgence and resummation, *Phys. Rev. Lett.* **115**, 072501 (2015).
  - [8] W. Florkowski, M. P. Heller, and M. Spaliński, New theories of relativistic hydrodynamics in the LHC era, *Rep. Prog. Phys.* **81**, 046001 (2018).
  - [9] W. Busza, K. Rajagopal, and W. van der Schee, Heavy ion collisions: The big picture and the big questions, *Annu. Rev. Nucl. Part. Sci.* **68**, 339 (2018).
  - [10] G. Giacalone, A. Mazeliauskas, and S. Schlichting, Hydrodynamic attractors, initial state energy, and particle production in relativistic nuclear collisions, *Phys. Rev. Lett.* **123**, 262301 (2019).
  - [11] B. Schenke, The smallest fluid on Earth, *Rep. Prog. Phys.* **84**, 082301 (2021).
  - [12] J. Berges, M. P. Heller, A. Mazeliauskas, and R. Venugopalan, QCD thermalization: Ab initio approaches and interdisciplinary connections, *Rev. Mod. Phys.* **93**, 035003 (2021).
  - [13] T. Kinoshita, T. Wenger, and D. S. Weiss, A quantum Newton's cradle, *Nature* **440**, 900 (2006).
  - [14] Y. Tang, W. Kao, K.-Y. Li, S. Seo, K. Mallayya, M. Rigol, S. Gopalakrishnan, and B. L. Lev, Thermalization near integrability in a dipolar quantum newton's cradle, *Phys. Rev. X* **8**, 021030 (2018).
  - [15] T. Kinoshita, T. Wenger, and D. S. Weiss, All-optical Bose-Einstein condensation using a compressible crossed dipole trap, *Phys. Rev. A* **71**, 011602 (2005).
  - [16] E. H. Lieb and W. Liniger, Exact analysis of an interacting Bose gas. I. The general solution and the ground state, *Phys. Rev.* **130**, 1605 (1963).
  - [17] M. Olshanii, Atomic scattering in the presence of an external confinement and a gas of impenetrable bosons, *Phys. Rev. Lett.* **81**, 938 (1998).
  - [18] C. N. Yang and C. P. Yang, Thermodynamics of a one-dimensional system of bosons with repulsive delta-function interaction, *J. Math. Phys.* **10**, 1115 (1969).
  - [19] M. Rigol and A. Muramatsu, Ground-state properties of hard-core bosons confined on one-dimensional optical lattices, *Phys. Rev. A* **72**, 013604 (2005).
  - [20] I. Bloch, J. Dalibard, and W. Zwerger, Many-body physics with ultracold gases, *Rev. Mod. Phys.* **80**, 885 (2008).
  - [21] P. Jordan and E. Wigner, Über das Paulische Äquivalenzverbot, *Z. Phys.* **47**, 631 (1928).
  - [22] M. Rigol and A. Muramatsu, Free expansion of impenetrable bosons on one-dimensional optical lattices, *Mod. Phys. Lett.* **19**, 861 (2005).
  - [23] R. van den Berg, B. Wouters, S. Eliëns, J. De Nardis, R. M. Konik, and J.-S. Caux, Separation of time scales in a quantum Newton's cradle, *Phys. Rev. Lett.* **116**, 225302 (2016).
  - [24] S. Wu, Y.-J. Wang, Q. Diot, and M. Prentiss, Splitting matter waves using an optimized standing-wave light-pulse sequence, *Phys. Rev. A* **71**, 043602 (2005).
  - [25] M. Rigol, V. Dunjko, V. Yurovsky, and M. Olshanii, Relaxation in a completely integrable many-body quantum system: An ab initio study of the dynamics of the highly excited states of 1d lattice hard-core bosons, *Phys. Rev. Lett.* **98**, 050405 (2007).
  - [26] E. Ilievski, J. De Nardis, B. Wouters, J.-S. Caux, F. H. L. Essler, and T. Prosen, Complete generalized Gibbs ensembles in an interacting theory, *Phys. Rev. Lett.* **115**,



- 157201 (2015).
- [27] L. Vidmar and M. Rigol, Generalized Gibbs ensemble in integrable lattice models, *J. Stat. Mech.* **2016**, 064007.
- [28] P. Calabrese, F. H. L. Essler, and G. Mussardo, Introduction to ‘Quantum Integrability in Out of Equilibrium Systems’, *J. Stat. Mech.* **2016**, 064001.
- [29] O. A. Castro-Alvaredo, B. Doyon, and T. Yoshimura, Emergent hydrodynamics in integrable quantum systems out of equilibrium, *Phys. Rev. X* **6**, 041065 (2016).
- [30] B. Bertini, M. Collura, J. De Nardis, and M. Fagotti, Transport in out-of-equilibrium XXZ chains: Exact profiles of charges and currents, *Phys. Rev. Lett.* **117**, 207201 (2016).
- [31] B. Doyon, Lecture notes on Generalised Hydrodynamics, *SciPost Phys. Lect. Notes* **18** (2020).
- [32] V. Alba, B. Bertini, M. Fagotti, L. Piroli, and P. Ruggero, Generalized-hydrodynamic approach to inhomogeneous quenches: correlations, entanglement and quantum effects, *J. Stat. Mech.* **2021**, 114004.
- [33] A. Bastianello, B. Bertini, B. Doyon, and R. Vasseur, Introduction to the special issue on emergent hydrodynamics in integrable many-body systems, *J. Stat. Mech.* **2022**, 014001.
- [34] M. Schemmer, I. Bouchoule, B. Doyon, and J. Dubail, Generalized hydrodynamics on an atom chip, *Phys. Rev. Lett.* **122**, 090601 (2019).
- [35] N. Malvania, Y. Zhang, Y. Le, J. Dubail, M. Rigol, and D. S. Weiss, Generalized hydrodynamics in strongly interacting 1D Bose gases, *Science* **373**, 1129 (2021).
- [36] F. Møller, C. Li, I. Mazets, H.-P. Stimming, T. Zhou, Z. Zhu, X. Chen, and J. Schmiedmayer, Extension of the generalized hydrodynamics to the dimensional crossover regime, *Phys. Rev. Lett.* **126**, 090602 (2021).
- [37] F. Cataldini, F. Møller, M. Tajik, J. a. Sabino, S.-C. Ji, I. Mazets, T. Schweigler, B. Rauer, and J. Schmiedmayer, Emergent Pauli blocking in a weakly interacting Bose gas, *Phys. Rev. X* **12**, 041032 (2022).
- [38] K. Yang, Y. Zhang, K.-Y. Li, K.-Y. Lin, S. Gopalakrishnan, M. Rigol, and B. L. Lev, Phantom energy in the nonlinear response of a quantum many-body scar state (2023), [arXiv:2308.11615](https://arxiv.org/abs/2308.11615).
- [39] M. Rigol, A. Muramatsu, and M. Olshanii, Hard-core bosons on optical superlattices: Dynamics and relaxation in the superfluid and insulating regimes, *Phys. Rev. A* **74**, 053616 (2006).
- [40] C. Gramsch and M. Rigol, Quenches in a quasidisordered integrable lattice system: Dynamics and statistical description of observables after relaxation, *Phys. Rev. A* **86**, 053615 (2012).
- [41] M. A. Cazalilla, Effect of suddenly turning on interactions in the luttinger model, *Phys. Rev. Lett.* **97**, 156403 (2006).
- [42] P. Calabrese, F. H. L. Essler, and M. Fagotti, Quantum quench in the transverse-field ising chain, *Phys. Rev. Lett.* **106**, 227203 (2011).
- [43] M. Fagotti and F. H. L. Essler, Reduced density matrix after a quantum quench, *Phys. Rev. B* **87**, 245107 (2013).
- [44] Y. Zhang, L. Vidmar, and M. Rigol, Statistical properties of the off-diagonal matrix elements of observables in eigenstates of integrable systems, *Phys. Rev. E* **106**, 014132 (2022).
- [45] M. Cramer, C. M. Dawson, J. Eisert, and T. J. Osborne, Exact relaxation in a class of nonequilibrium quantum lattice systems, *Phys. Rev. Lett.* **100**, 030602 (2008).
- [46] M. Gluza, C. Krumnow, M. Friesdorf, C. Gogolin, and J. Eisert, Equilibration via Gaussification in fermionic lattice systems, *Phys. Rev. Lett.* **117**, 190602 (2016).
- [47] C. Murthy and M. Srednicki, Relaxation to Gaussian and generalized Gibbs states in systems of particles with quadratic Hamiltonians, *Phys. Rev. E* **100**, 012146 (2019).
- [48] M. Gluza, J. Eisert, and T. Farrelly, Equilibration towards generalized Gibbs ensembles in non-interacting theories, *SciPost Phys.* **7**, 038 (2019).
- [49] P. Łydzba, M. Mierzejewski, M. Rigol, and L. Vidmar, Generalized thermalization in quantum-chaotic quadratic Hamiltonians, *Phys. Rev. Lett.* **131**, 060401 (2023).
- [50] A. C. Cassidy, C. W. Clark, and M. Rigol, Generalized thermalization in an integrable lattice system, *Phys. Rev. Lett.* **106**, 140405 (2011).
- [51] J.-S. Caux and F. H. L. Essler, Time evolution of local observables after quenching to an integrable model, *Phys. Rev. Lett.* **110**, 257203 (2013).
- [52] B. Pozsgay, Quantum quenches and generalized Gibbs ensemble in a Bethe ansatz solvable lattice model of interacting bosons, *J. Stat. Mech.* **2014**, P10045.
- [53] T. Ishii and T. Mori, Strong eigenstate thermalization within a generalized shell in noninteracting integrable systems, *Phys. Rev. E* **100**, 012139 (2019).
- [54] A. Dymarsky and K. Pavlenko, Generalized eigenstate thermalization hypothesis in 2D conformal field theories, *Phys. Rev. Lett.* **123**, 111602 (2019).
- [55] G. Policastro, D. T. Son, and A. O. Starinets, Shear viscosity of strongly coupled  $n = 4$  supersymmetric yang-mills plasma, *Phys. Rev. Lett.* **87**, 081601 (2001).
- [56] A. Cabo and M. Rigol, Constituent quark masses from modified perturbative QCD, *Eur. Phys. J. C* **23**, 289 (2002).
- [57] M. Rigol and A. Cabo, Modified initial state for perturbative QCD, *Phys. Rev. D* **62**, 074018 (2000).
- [58] M. Rigol and M. Fitzpatrick, Initial-state dependence of the quench dynamics in integrable quantum systems, *Phys. Rev. A* **84**, 033640 (2011).
- [59] C. Eigen, J. A. P. Glidden, R. Lopes, E. A. Cornell, R. P. Smith, and Z. Hadzibabic, Universal prethermal dynamics of Bose gases quenched to unitarity, *Nature* **563**, 221 (2018).
- [60] X. Yin and L. Radzihovsky, Quench dynamics of a strongly interacting resonant Bose gas, *Phys. Rev. A* **88**, 063611 (2013).